Award Number: 06HQGR0042

SIMULATING FORWARD AND BACKWARD SCATTERING IN VISCOELASTIC 3D MEDIA WITH RANDOM VELOCITY VARIATIONS AND BASIN STRUCTURE

FINAL REPORT

March 31, 2009

A. Pitarka and G. Ichinose

URS Group, Inc.

566 El Dorado Street - 2nd Floor
Pasadena CA 91101

Tel: 626.449.7650
Fax: 626.449.3536

Email: paul_somerville@urscorp.com

Research supported by the U.S. Geological Survey (USGS), Department of the Interior, under award number 06HQGR0042. The views and conclusions contained in this document are those of the authors and should not be interpreted as necessarily representing the official policies, either expressed or implied, of the U.S. Government.

Simulating Forward and Backward Scattering in Viscoelastic 3D Media With Random Velocity Variations and Basin Structure

Arben Pitarka and Gene Ichinose
URS Group, Inc.

Introduction

The influence of random heterogeneities and rough free surface on coda wave formation have been shown to be significant (Aki and Chouet, 1975; Saito *et al*., 2003; Dainty, 1984; Frankel and Wennerberg, 1987; Zeng *et al*., 1991; Zeng 1993). This very important phenomenon needs to be investigated by both observational and numerical techniques. While analyses of recorded seismograms can reveal the degree of complexity in the crust and the effect of small-scale and large-scale perturbation on different wave phases, numerical experiments can be used for isolating effects caused by the wave path, seismic source, and local structure. They can also be used to verify hypothesis that are at the foundation of wave scattering models. A considerable body of knowledge about the effects of scattering and anelastic attenuation has been gained from nuclear explosion monitoring research, especially for resolving the generation of high frequency shear waves and Lg coda waves during underground explosions and high frequency Lg wave blockage (e.g., Mitchell *et al*. 1995; Dainty, 1996; Wu *et al*., 2000; Myers *et al*., 2005; Xie *et al*., 2005; Pitarka *et al*., 2008).

The main purpose of this study is to analyze and evaluate the effects of wave propagation scattering through step-by-step numerical experiments and waveform modeling, with the goal of providing useful insights into ongoing research for development of simple empirical models of scattering that can be used in broad-band ground motion simulation techniques (Hartzell *et al*., 1999; Liu *et al*., 2006; Graves and Pitarka, 2004; Pitarka *et al*, 2000; Zeng *et al*., 1994; Zeng *et al*., 1995). We investigated the effect of shallow crustal heterogeneities on 3D wave propagation scattering by applying an anelastic finite-difference wave propagation modeling method and three-dimensional crustal models with random perturbations. We performed simulations of wave propagation in highly heterogeneous media for a range of source depths, receiver distances and source types. In the first stage of our study, we investigated the effect of small-scale crustal heterogeneities on wave propagation scattering. Our numerical experiments with 3D velocity models that include random velocity perturbations and microbasins, designed to produce wave scattering in the upper 5km of the crust, clearly show that wave-path scattering alone can produce P, S and Lg coda waves with significant energy. During the second stage we investigated the effect of surface topography combined with crustal heterogeneities on wave propagation scattering. The topography elevation was simulated using correlated random variations along the free surface.

The wave-path scattering effects were also investigated by simulating observed high frequency source directivity effects, as well as fault zone wave trapping in highly fractured conditions from aftershocks of the Big Bear, California earthquake sequence. In our simulations of wave propagation we used a finite difference computer program using the computer cluster at Caltech. The seismograms were calculated up to 3.5Hz, and for epicentral distances up to 300km.

Our simulations show that the surface topography increases the wave-path scattering effects. The combined effects of crustal heterogeneities and surface topography produce P and S coda waves with significant energy even for isotropic explosion sources which do not generate shear waves. The energy of coda waves depends on the source depth. P/Lg ratios estimated at different frequencies indicate that the wave scattering also depends on the source type, especially at high frequencies.

Figure 1 shows the effect of a 1600m thick sedimentary basin on the surface recorded S-wave coda energy envelope. The site is in the Osaka region of Japan. In comparison to the 2001 m deep borehole recording, the surface recording shows significantly low apparent Q^{-1} scattering effects at 1-2Hz early in the S-wave coda over a duration of approximately 40sec. At high frequencies the differences in energy envelopes begin to converge at about ~7-12Hz. We also notice that the duration of the apparently low scattering Q decreases with decreasing magnitude.

Separating basin reverberations from scattering and attenuation effects from random velocity perturbations is important for strong ground motion modeling. Much of the seismic hazard in the United States is due to long duration shaking in heavily populated sedimentary basins, such as the Santa Clara, Los Angeles, Seattle-Tacoma, Willamette Valley, and Salt Lake City basins, and the Mississippi embayment. This is manifested in damaging ground motions caused by the 1994 Northridge earthquake (e.g., Pitarka and Irikura, 1996a). It is therefore important to understand the relative contributions of scattering effects and basin effects, so that they can be used to improve our methods to simulate strong ground shaking.

1. Observed Regional Seismic Wave Propagation Scattering

We analyzed scattering effects on recorded regional seismograms from earthquakes in South Korea. In particular we analyzed envelopes of broad-band velocity seismograms in different frequency bands, recorded at stations near nodal planes. Near nodal planes the coda of P and S waves are both direct products of wave scattering. Therefore the comparison of the three components of motion at such stations could give useful information about the size of random structural complexities responsible for the observed coda waves. This information is crucial in guiding the development of a scheme that was used to model random spatial perturbations of the velocity.

We investigated the amplitude variation of the ground velocity envelope as a function of frequency from the Mw 4.5 070120 earthquake in South Korea. We used broad-band recordings at station CHC, CHJ, ULJ, and SES. The station and the earthquake locations are shown in Figure 2. The earthquake was located at a depth of 11km. Its focal mechanism (strike=209°, dip=90°, rake=180°) was determined using a cut and paste (CAP) inversion technique that is based on different weights for relatively high frequency waveform modeling of Pnl and relatively long period surface waves (Tan *et al*., 2006). The pure strike-slip mechanism of the earthquake and its recording at stations near the P wave nodal planes make it ideal for analyzing regional scattered waves. Figure 3 shows the amplitude variation of the ground velocity envelope as a function of frequency at four stations. Stations CHJ and CHC are close to P-wave nodal planes. At these stations the tangential component of motion is much higher than the two

others. The epicentral distance of the considered stations varies from 69km at CHJ to 214km at SES.

Several general observations relevant to the wave scattering can be made. First, the relatively large amplitude of the direct P wave on the vertical and radial components observed at the non-nodal stations ULJ and SES remains significant even at frequencies higher then 8Hz. This indicates that the radiation pattern of the P waves is effective even at such high frequencies. In contrast, the P wave scattering, expressed as the relative increase of amplitude of the P wave and its coda in the tangential component of motion at P-wave nodal stations, becomes significant at frequencies higher than 4Hz. Note the relatively large amplitude of P coda waves on the tangential component at such frequencies. This indicates that P to S-wave conversions are significant at high frequencies. As will be shown later, scattering effects due to small-scale perturbations in the shallow crust cause a similar increase in amplitude of high frequency P-wave coda in all three components. Changes in the amplitudes of P waves and their coda as a function of frequency could be very helpful in constraining the basic parameters of scattering models.

Second, because of their shorter wavelength, S waves are more susceptible to wave propagation scattering effects. As shown in Figure 3, for such waves the amplitude difference between the three components that is controlled by the source radiation pattern is observed only at frequencies lower than 2Hz. At frequencies higher than 4Hz, and independently of the epicentral distance, the amplitude of S wave coda is the same for all three components. This suggests that at high frequencies the amplitude of S wave coda does not follow the source radiation pattern. This example shows that at high frequencies the S wave radiation pattern is mainly controlled by wave scattering in the crust. This very robust feature of S coda waves can be used to derive stable estimates of source parameters.

We also observed that the ratio between Pn and Pg seems to be stable over different frequencies. For strike slip events such as the 070120 Korean earthquake, Pn should be much smaller than Pg because of its steeper takeoff angle. But for explosions, Pn and Pg seem to have similar amplitudes (Kim and Richards, 2007). For the Korean earthquake, Pn is indeed much weaker than Pg for all the frequency bands, suggesting that the ratio between Pn and Pg can be used to constrain source mechanisms even at high frequencies.

1. The source radiation pattern of P waves starts to break down only at above 8Hz.

2. There is a significant increase in amplitude of P coda waves in the tangential component above 4Hz due to P-S conversions.

3. S waves are more susceptible to wave propagation scattering than P waves. The radiation pattern effect of S waves is largely distorted at frequencies above 2Hz. At these frequencies the amplitudes of all three components becomes similar.

2. Observed Scattering Effects on Waveforms from Earthquakes and Explosions

The origin of the high frequency scattering affecting mainly the P, Rg and Lg coda waves (above 1Hz) could be due to either deep or shallow crustal structure complexities along the wave path or

in the source region (e.g., Aki, 1969; Dainty, 1996; Wu *et al*., 2000, He *et al*., 2008). Several studies have shown that Lg wave scattering is related to small-scale structural heterogeneities. Other causes of scattering could also be large-scale structural complexities such as crustal thinning or multipathing in the crust and large basins (e.g. Ni and Barazangi, 1983; Phillips *et al*., 2000).

We investigated the effect of wave scattering on broad-band waveforms in connection with source depth and distance. We analyzed smoothed waveform envelopes from the North Korean explosion and the 020416 M4.5 earthquake in North Korea recorded at close and intermediate distances, about 100km for STATION1 and 400km for MDJ, respectively. The earthquake, explosion and stations location are shown in Figure 4. STATION 1 which is not shown in this figure is located south west of MDJ. The epicentral distance between the earthquake and explosion is about 60km. Knowing that the geological structures along the azimuthal direction of the two stations are very different, it is expected that the wave scattering will have different effects on the corresponding waveforms. However we want to see whether or not such effects are also dependent on distance, source depth and wave type.

Figure 5a shows smoothed envelopes of broad-band velocity seismograms from the 020416 earthquake recorded at station MDJ and STATION 1. The envelopes are calculated in the frequency bands of 0.8-2Hz and 4-8Hz. An interesting feature of the envelopes is the decay rate of P coda waves. At STATION1, which is closer to the source, the decay rate of P coda wave amplitude is much higher than that at MDJ. P to S wave conversions due to structural complexities and the complex free surface geometry provide more energy to P coda waves. The recording at MDJ shows that this scattering effect increases with distance. Also, in contrast with MDJ, at STATION1 the amplitude ratio between P and S waves does not change with frequency. This tells us that wave scattering at short distances has similar effects on direct P and S waves. These observations suggest that in this region, the wave propagation scattering is azimuthally dependent. Scattering is stronger on the S wave than on the P wave and along the path to MDJ which is also the longest. As a consequence the S/P ratio at MDJ is strongly reduced at high frequencies in all three components.

It is interesting to see whether such effects depend on the source type. We performed the same analyses on the explosion waveforms at MDJ and STATION1. Figure 5b shows smoothed waveform envelopes for the 061009 North Korean explosion calculated at MDJ and STATION1. The explosion waveforms are rich in S wave energy, in particular at STATION1 which is closer to the source. The difference in wave scattering between the two stations observed during the earthquake remains visible even for the explosion source. The similarities between the explosion and earthquake suggest that the observed difference in scattering effects between the two stations is rather shallow and not strictly related to the source region.

The comparison of waveform envelopes between the earthquake and explosion is shown in Figure 5c. Along the short wave path to STATION1, with low wave path scattering, P/S coda wave amplitude ratios for the earthquake and explosion are very similar. In contrast, along the wave-path to MDJ which is longer and has strong wave scattering, the P/S ratios between the earthquake and explosion are very different. The P/S ratio for the explosion at MDJ is much larger. These observations suggest that at large epicentral distances, the cumulative effect of

wave scattering on P waves is enhanced. This observation is very well reproduced by our subsequent simulations of 3D wave scattering.

3. Fault Zone Wave Scattering: Big Bear, California Earthquake Sequence

Near-source wave scattering has strong implications for shaping the source energy radiation at local and teleseismic distances. It also affects the amplitude of depth phases. Due to limited knowledge of small-scale crustal heterogeneities and insufficient near-source recorded waveform data, source region wave scattering is often neglected in studies of focal mechanism and magnitude estimates, in particular for events located in tectonically complex regions. Two types of source region scattering are relevant to our study. The first is fault zone wave scattering, a well known phenomena that has been the focus of many recent studies (e.g., Ben-Zion, 1998; Ben-Zion *et al*., 2007). The second is scattering due to local topography and microbasins near shallow seismic sources.

Several studies have shown strong evidence of fault zone wave scattering, also described as fault zone trapped waves. Most of them are focused on near-fault ground motion characteristics. By using very high quality data, Tan and Helmberger (2009) have been able to demonstrate significant effects of fault zone complexities on rupture characteristics. Their waveform cross correlation analysis can potentially be used as a diagnostic tool for detecting fault zone effects on P and S coda waves at regional distances. Here we briefly describe the essence of their study and its implications for understanding fault zone scattering.

Tan and Helmberger (2009) analyzed broad-band waveform data to infer focal mechanism, rupture directivity, kinematic rupture, and stress drop parameters for a large number of earthquakes from the 2003 Big Bear earthquake sequence (Figure 6). Their technique uses small events as Empirical Green's functions to calculate Relative Source Time Functions (RSTF). RSTF's are then used to derive the rupture directivity. Figure 7 shows inferred rupture direction for selected events. For these events the rupture planes have complex orientation indicating complex faulting. In particular, ruptures propagate in all directions, with wide-ranging rupture speeds. For example, although they are closely located, the neighboring events 13935996 and 13936596 rupture on conjugate fault planes, suggesting cross-over faults at depth. Besides, events that are both located on the main shock fault plane, e.g., 13937492 and 13935996, rupture in opposite directions, which indicates heterogeneity of the fault plane or complexity of the fault zone.

The Big Bear earthquake sequence shows a clear relationship between the relative location of small earthquakes with respect to the mainshock and their source characteristics. Small events located near the main event (NF) have relatively low stress drop and relatively large rupture velocity and fault length compared to more distant cross-fault events (DF) to the north. The NF events display more complexities between the P-wave-train and S-wave-train. Many of these events have relatively complex S-waves compared to the DF events. The P-waves seem relatively stable since they were able predict the differences based on directivity estimates and fault parameters.

However, many of the S-waves are observationally more complex when we applied waveform intercorrelation (Lay *et al*., 1984) between an event located inside the fault zone and an event located outside the fault zone (Figure 8). As shown in this figure, the quality of the intercorrelation at station DPP for event 1396326 and event 13937600 is different for P waves and S waves. This suggests that these complexities are caused by wave propagation scattering in the fault damage zone where the sources are located. The small scale heterogeneities affect the S waves more than the P waves which have longer wavelengths. We infer that this feature is caused by fault-zone damage where energy is locally trapped in the slow leaky waveguide and then re-radiated from the lateral edges of the fault zone. In a subsequent section we will show results of our modeling of fault zone wave scattering. As will be shown in a subsequent section of this study, our 3D numerical simulation results demonstrate the implications of fault zone damage for observed waveform scattering of P and S waves.

4. Simulation of 3D Wave Scattering Using Finite-Difference Method

Early studies on attenuation demonstrated that velocity fluctuations with alternating high and low velocity layers, similar to those found in well logs, are most effective in removing high frequencies from the earliest portion of the transmitted wave train (e.g. Saikia, 2006). We used velocity fluctuations in 3D media to duplicate this feature commonly observed geologically in stratigraphy as alternating layers of shale and sandstones in sedimentary layers or alternating layers of gabbro and granite in bedrock.

The influence of crustal random heterogeneities of all scales and surface topography are shown to be very important factors influencing the scattered waves observed as coda waves. Because of their robust characteristics, coda waves have been successfully used to calculate with high accuracy the magnitude of seismic events (Mayeda *et al*., 2003). While analyses of recorded seismograms can reveal the degree of complexity in the crust and the effect of small scale and large- scale perturbation on different wave phases, the numerical experiments can be used for isolating effects caused by the wave path, seismic source, and local structure.

Studies of wave propagation based on three-dimensional finite-difference methods (3D-FDM) have contributed to a better understanding of the heterogeneous path and source process (Myers *et al*., 2003; Pitarka *et al*., 1998, Graves *et al*., 1998; Graves and Pitarka 2004; Frankel and Vidale, 1992; McLaughlin *et al*., 1993). A common feature of the 3D-FDM techniques applied in most of these studies is the use of the uniform-grid formulation with constant grid spacing, which requires relatively large computer memory. Due to computational limitations, these studies are restricted to long periods (usually longer than 1s), and use relatively high values for the shear velocity of the near-surface sediments. 3D-FDM techniques capable of extending these calculations to shorter period seismograms at large distances without additional computer memory are essential to understand the influence of the propagation model in the regions where geologic features are complex. A significant improvement in the 3D finite-difference technique was made by the application of finite-difference operators on 3D grids with variable spacing (Pitarka, 1999). This, combined with parallel processing, enables the modeling of wave propagation at high frequencies using realistic crustal velocity models. Our 3D-FDM computer code solves the stress-velocity equations in a heterogeneous medium using staggered grids based on such a technique. The code can also treat heterogeneous structure with surface topography

and rupture dynamics as well (Pitarka and Irikura, 1996b, and Pitarka and Dalguer, 2003). The technique is an excellent approach to modeling complex wave propagation in regional settings.

In this study we apply a 3D staggered grid finite difference technique and a grid with variable spacing (Pitarka, 1999) to simulate the effect of surface topography and shallow crustal heterogeneity on wave propagation scattering on both isotropic explosion and earthquake sources. Our finite difference code solves the stress-velocity wave equations in a heterogeneous medium using staggered grids. Anelastic attenuation is implemented efficiently using relaxation times between stress and strain based on the viscoelastic modulus representation (e.g., Day and Bradley, 2001; Graves and Day, 2003). The technique for generating the 3D velocity model on a regular grid with variable spacing allows for inclusion of small-scale complexities and surface topography as well. The technique we use to model free surface topography is an extension of the formalism that we have applied to modeling wave propagation in media with a curved free surface (Pitarka and Irikura, 1996b). The performance of our free-surface boundary condition technique at handling Lg coda waves for flat free surface and very long distances was compared with that of the FK method of Saikia (1994) for a shallow source. Also the technique has been validated against other standard and accurate techniques for modeling surface topography such as the 2D Boundary Element Method (BEM) and the 2D-Discrete Wavenumber Boundary Integral Equation method of Takenaka *et al*. (1996).

Parameterization of Scattering Model

The wave scattering effects in our 3D simulations are modeled by random perturbations of the velocity. The perturbations expressed in percentage of unperturbed shear-wave velocity are spatially correlated using a correlation length. Results of sensitivity analyses with different velocity perturbations and correlation lengths, not shown here, confirm the importance of these parameters in producing realistic wave path scattering over a broad frequency range. One way of deriving realistic scattering model parameters is to simulate observed broad-band waveforms from small and moderate regional earthquakes using random perturbations of well calibrated velocity models. The objective of such modeling is to derive scattering parameterization of the velocity model by reproducing the gradual disappearance of the observed radiation pattern of P and S waves with increasing frequency. This is known to be caused by near-source and wave-path scattering. The use of both P and S waves as well as their respective coda decay provides excellent empirical constraints on deriving realistic random velocity perturbations with correct correlation lengths.

In our scheme for generating the velocity perturbation of the 3D velocity model, a random number generator is used to assign a velocity perturbation to each point in the 3D grid. Originally we had planed to use 3D random media following the three types used by Frankel and Clayton (1986). The correlation functions for the Von Karman, exponential, and Gaussian functions represent these types of media statistically. The Fourier transforms of the correlation functions represent the power spectrum density of the medium fluctuations. Figure 9 shows three-dimensional media with random velocity variations based on exponential and von Karman functions.

In 2D the Gaussian and exponential functions require a small computer memory even for large models. However 2D Fourier transforms are computationally expensive, especially for regional velocity models. An alternative method that yields random perturbations of the velocity model with similar statistical properties is the technique we have applied in this study. The spatial perturbation of velocity in our 3D random model is expressed in percentage of unperturbed shear modulus μ. The random perturbations are inter-correlated using a spatial correlation length D. The perturbed shear modulus μ^* at a given grid node 'k' is calculated using the following equation:

$$\mu_k^* = \mu_k(1 + 0.10 f_k)$$

where :

$$f_k = \frac{\sum_1^N \omega_i * rand_i}{W_k} \qquad W_k = \sum_1^N \omega_i \qquad \omega_i = \exp(-d_i^2 / D^2)$$

- $rand_i$:a spatial distribution of real random numbers ranging between -1 and 1.
- d_i : distance between the given node 'k' and adjacent nodes located within an ellipsoid centered at node 'k' with horizontal long axis D and short axis D/2.
- D : correlation length. D = 1.5km.

The wave scattering effects in our 3D simulations are modeled by random perturbations of the velocity. The perturbations expressed in percentage of unperturbed shear-wave velocity are inter-correlated using a spatial correlation length. The scattering parameters such as the amount of perturbation (in this case 10%) and its correlation length were derived previously. A velocity perturbation of up to 10% with a correlation length of 1.5km was found to correctly reproduce the observed P and S coda wave decay, and the disappearance of their corresponding frequency-dependent radiation pattern. This simple scheme is far less time consuming than the other scheme which uses 3D Fourier transforms. A similar approach is used to generate the surface topography. A typical velocity model with irregular surface topography and random velocity perturbations used in this study is illustrated in Figure 10. In this model the maximum elevation is 1400m, and the correlation length of the topographic random variations is 3km.

5. Effect of Seismic Source Depth on Simulated Wave Scattering

Extensive analyses of short-period teleseismic P-waves from NTS explosions performed by Lay (1991) in the time domain and Gupta *et al.* (1987) in the frequency domain reveal that the deeper events are simpler than the shallower ones. They both suggest that this could be caused by the increased scattering of shallow complex structure as proposed by McLaughlin *et al*. (1986). Some detailed 2D modeling studies for Yucca Flats events support this interpretation (e.g., Stead, 1989; Stead and Helmberger, 1988).

We have examined the combined effects of wave propagation scattering due to complexities in the shallow crust and surface topography in relation with the source depth. These effects were investigated by calculating synthetic seismograms for two double couple point sources located at

depths of 2km and 10km. The velocity model used in the simulations is shown in Figure 10. The small-scale variations of the velocity are randomly distributed along the top 5km of the crust. The velocity fluctuations are in the range of 2-10% and their correlation length is 3km. In addition to small-scale fluctuations, our velocity model includes several microbasins with sizes varying between 20-40km and depth up to 3.5km. The elevation of surface topography varies between 0 and 1400m. The correlation length of topographic random variations is 1.5km. The selected minimum grid spacing of 200m ensures accurate wave propagation modeling up to 1.8Hz. The ground motion velocity was computed on a linear array of stations located on the free surface. The stations spacing is 4km, and the maximum epicentral distance is 130km. As shown in Figure 10, several stations are located in basins.

We investigated the relative contribution of wave-field scattering in different frequency bands. The comparison between the two scenarios is shown in Figure 11. Figure 11 shows the vertical component of synthetic velocity time histories band-pass filtered at two frequency bands, 0-1Hz and 1-1.8Hz. At low frequencies (< 1Hz) the waveforms are dominated by the S wave and surface waves for both the deep and shallow sources. However the amplitude and duration of the surface waves are very different between the two sources. As a result of a cumulative scattering effect and probably better trapping of converted waves at the free surface in the shallow crust, the shallow source generates coda waves with longer duration. This feature is more distinctive at basin sites (blue traces in Figure 11). However, at higher frequencies (> 1Hz) these differences are insignificant. This is clearly seen in Figure 12, where we compare the S wave coda in smoothed envelopes of waveforms calculated at stations S16 and S26. The difference in the envelope slope for scattered S waves between deep and shallow sources is noticeable only at low frequencies (<1Hz). At high frequencies the slope remains unchanged at both sites, suggesting a stable shallow scattering effect. This result suggests that in relation to source depth, high frequency scattering is more stable than the low frequency scattering. Therefore the slope of the smoothed envelope of the low frequency part of the signal could be used to distinguish between shallow and deep events.

6. Effect of Source Type: Comparison of Earthquakes and Explosion

Finally, using 3D modeling we investigated the effect of scattering on Lg and coda wave propagation due to the topography above the source as a function of frequency band and source depth. For this experiment we generated regional and far-regional seismograms for explosion sources and examined physical conditions related to scattering that can excite S waves. (Stead, 1989; Saikia *et al*., 2001, Stevens *et al*., 2003; Rodgers and Tromp, 2005). Our point source model did not include spall (e.g. Day and McLaughlin, 1991; Patton and Taylor, 1995)

Aiming at understanding scattering effects in relation to source type, we performed simulations for an isotropic explosion point source located at a depth of 400m, and an earthquake double-couple point source located at a depth of 2km. The source location and station locations are shown in Figure 10. Since we are investigating the mechanisms of S wave generation not related to the source, we used an isotropic explosion point source. The source time function for both earthquake and explosion has a flat spectrum in the considered frequency range. The source time function for the earthquake is a “bell-shape” and for the explosion is a modified Haskell type.

Figure 13 shows the comparison of the vertical component of velocity seismograms calculated at a linear array of stations crossing two basins (see Figure 10). We observed the relative amplitude of P and S coda waves in the frequency ranges of 0.1-1.0Hz and 1.0-1.8Hz.

Both sources generate S coda and Rg waves that are energetic even at short distances. The effects of shallow heterogeneities and surface topography on wave type conversions such as P to S and S to P as well Rg surface waves are very impressive, especially for the explosion source. Our numerical experiment clearly shows that wave-path scattering alone caused by rough topography and crustal heterogeneities can produce S coda waves with significant energy even for the explosion sources. It is important to note that P coda waves become more energetic at longer distances. The Rg wave dominates the later phases in explosion seismograms. Their amplitude is larger than that of the direct P wave. However at high frequencies (above 1Hz) the Rg waves quickly attenuate with distance. Because of the Rg to Lg conversions caused by the surface topography, the amplitude of Rg waves at longer distances is comparable with that of the P waves.

Our simulations suggest that the amplitude ratio between P and Rg coda waves is still higher for the explosion source at high frequencies. They clearly show that because S coda waves have shorter wavelength their amplitude diminishes faster than that of P coda waves at long distances. This result is in agreement with observations made when we compared the North Korean explosion and a nearby earthquake at short and regional distances.

As demonstrated by the comparison of smoothed envelopes of waveforms calculated at two selected stations (Figure 14), P coda waves from the explosion have relatively large amplitudes compared to P coda waves from the earthquake. The cumulative effect of scattering caused by the surface topography and spatial structural heterogeneities contribute to the generation of P coda waves through P/S and S/P conversions. Unlike for low frequencies, the difference of P/Rg ratio between the explosion and the earthquake source is significant at high frequencies. However, as we will later show, the difference becomes small when the earthquake is not very shallow and the explosion is not located near a complex boundary (e.g., Saikia, 1992).

7. Effects of Near-Source Structure and Fault Zone Structure on Near-Source Wave Scattering

Here we focus on wave propagation scattering caused by either strong near-source structural discontinuities such as basin edges with strong velocity contrast, fault zones with complex geometry, or near source topography. This type of scattering affects ground motion not only at near-source distances but also at regional distances (e.g., He *et al*., 2008; Lay and Welc, 1987; Langston, 1989). We modeled the effects of basin edge and fault zone trapped waves at short and intermediate distances (30 -150km).

Basin Edge Effects

In our investigation we used the 3D velocity model and receivers shown in Figure 10. We calculated two sets of synthetic seismograms (0.1-1.8Hz). One set is from an explosion source located near the basin edge, but outside the basin, referred as source RE, and the other set is from

an explosion source located near the basin edge inside the basin referred as source BE (Figure 15). Both sources have a depth of 400 m. The grid spacing in our finite difference calculations is 200m. Figure 16 compares the corresponding vertical component of synthetic velocity band pass filtered at 0.1-1Hz and 1.0-1.8Hz. There are clear waveform differences between the two sources especially at high frequencies (1.0-1.8Hz). The most significant one is the difference in amplitudes of P waves and P coda waves. The explosion outside the basin produces much larger P waves that are rich in high frequencies. In contrast the amplitude of the P wave and P coda waves is relatively small for the basin explosion. This behavior may be explained by the trapping and diffraction of short period P waves in the basin edge.

Meanwhile, the structural complexity at the basin edge increases the energy of S coda waves mainly due to P to S waves conversions. Besides being attenuated in the basin sediments, the P waves do not develop large coda waves as some of their energy, reflected at the free surface, leaks back to the underlying bedrock and deeper crust. As a consequence the waveforms from the basin explosion look very similar to those from an earthquake. Also the reduction of P/S ratio caused by basin edge effects makes it difficult to distinguish between the explosion and shallow earthquake. This is clearly seen in Figure 17 which compares smoothed envelopes of the vertical component of velocity at station S16 (rock site) and station S26 (basin site) calculated for an earthquake at a depth of 7km, an explosion located outside the basin, and an explosion located within the basin. At high frequencies (1-1.8Hz) there is a striking similarity between the earthquake and basin edge explosion in both the rock site and the basin site. Our simulation demonstrates that relative amplitude of P and Rg waves for explosion sources is sensitive to the source emplacement structural complexities. Our results suggest that because of basin edge effects, the energy of P coda waves for sources within the basin is strongly reduced due to near-source wave scattering.

Fault Zone Damage Effects

Fault zone effects on wave propagation have been observed and well recorded during large earthquakes. These observations reveal the complexity of the fault zone damage which could reach depths of 7-10km. Depending on the structural complexities of the fault zone and age of the faults the obvious effects of wave trapping within the fault zone have been shown to be significant at high frequencies and near-fault distances. It is only recently that studies of fault zone effects have been extended to smaller events and to regional distances. As we described in the previous section their observation shows that complex structure of tectonic regions not only affect the rupture dynamics it also affect the azimuthal distribution of radiated energy and rupture directivity. In addition, the effects are strong at high frequencies. The azimuthal dependency of this peculiar behavior need to be taken into account when broad band techniques are used to invert for focal mechanism and magnitude estimates of small events. Through 3D numerical simulations and using simple fault zone models, we demonstrate the implication of fault zone damage on observed waveform scattering of P and S waves.

Figure 18 shows the locations of a vertical fault zone, earthquake epicenter and two circular arrays of stations used in the simulation of velocity seismograms. We used a grid spacing of 40m which ensured accurate modeling up to 7Hz. The fault zone is 700m wide, and reaches a depth of 12km. The softer material within the fault zone is represented by random perturbations

of shear modulus up to 10% with a correlation length of 1km. In order to investigate the effects of scattering due to the fault zone, we calculated velocity seismograms from a pure strike slip earthquake rupturing a 1km x 1km fault area. The rupture starts near the southern edge of the fault and propagates toward the north. We considered three different fault locations, similar to the ones observed during the Big Bear earthquake sequence. In the first scenario the fault is located in the middle of the fault zone. In the second scenario the fault zone is located outside the fault zone on the east side 200m of the fault. The simulations for the third scenario were performed without the fault zone. The corresponding synthetic seismograms were used as a reference in the analyses of the rupture scenarios with fault zone effects. The comparison of transverse and vertical components of simulated velocity seismograms (0.1-7Hz) are shown in Figure 19.

Two interesting wave propagation phenomena are observed when the fault ruptures within the fault zone: First, ringing of the S waves caused by waves trapped within the fault zone is visible only at receivers located in front of the north tip of the fault zone (receivers 5, 6, and 7). A less visible ringing is observed after the P wave. It is mainly caused by trapped P waves and P to S converted waves. Second, very pronounced surface waves with long coda propagate away from the fault tip. They dominate the coda waves behind the S wave train. A slight decrease in the duration of the direct S wave pulse caused by the forward rupture directivity effect is seen at receiver 7.

These typical waveform characteristics are obviously not present when the fault zone is excluded, as demonstrated by the half space modeling results. When the earthquake ruptures adjacent to the fault zone the waveform complexities are still preserved. However the ringing phenomenon is weaker and the S coda waves at receivers on the opposite side of the fault zone are much smaller in amplitude. The most striking difference between the two scenarios is the duration of the direct S wave pulse. Our simulations suggest that when the earthquake is located within the fault zone the S wave pulse duration is much longer. Therefore S waves perturbed by the fault zone structure may not directly reflect the source rupture process. They tend to be contaminated by wave scattering which largely depends on the relative location of the fault with respect to the fault zone. Also our simulations suggest that the amplitude of coda waves from earthquakes near or in the fault zone depends on whether the fault zone reaches the free surface. Buried fault zones may not generate strong surface waves. Our fault zone model is far from being realistic, but nevertheless it underlines the significant effect of the source region wave scattering in regions with fault-damaged zones.

8. Rupture Directivity Effects in Media with Random Velocity Perturbations

Studies of local and regional waveforms from small earthquakes have demonstrated that rupture directivity has a significant effect over a broad frequency range. Forward rupture directivity affects the amplitude of seismic waves over this broad frequency range by increasing the amplitude of the ground motion in the direction of rupture propagation. In contrast, at sites in the backward rupture directivity, the ground motion amplitude is greatly reduced but the duration of the ground motion is increased. There have not been many studies of rupture directivity of small events especially at high frequencies. By using empirical Green's functions of small magnitude earthquakes, Tan and Helmberger (2009) were able to derive the rupture process of

earthquakes of the Big Bear sequence for magnitudes as small as M2.5. They found that the rupture directivity affects frequencies up to 7Hz.

In this study we investigate the effect of wave scattering on waveforms affected by rupture directivity during small earthquakes. We used two velocity models, one a horizontally layered model (1D model) and the other including random perturbations of velocity in the upper 6km of the horizontally layered model, and small shallow basins (3D model with scattering). The perturbations were designed to simulate wave scattering similar to the previous numerical experiments. We calculated synthetic waveforms from a double-couple point source with pure strike slip mechanism to maximize the directivity effect on the transverse component and an extended source containing 4 double-couple point sources with pure strike-slip mechanism, activated at equal time intervals to simulate unilateral rupture propagation. The sources are equally spaced at 400m. The rise time is 0.15sec, and rupture velocity is equal to 0.8 times the local shear wave velocity. The maximum frequency in our synthetic seismograms is 6.5Hz.

Figure 20a shows an overview of the top part of the model with locations of the source and stations. In this figure we also compare the fault-normal component of velocity seismograms for the extended source rupturing toward the east and velocity seismograms for the reference double couple point source. The synthetic seismograms were calculated with the 1D model. Compared to the single point source model, the extended source model generates slightly reduced high frequency amplitudes, especially at receivers on the west of the source (rec: 6, 5, 4, 3, 2, and 1). This well-known phenomenon is caused by destructive wave interference at high frequencies. At stations affected by the forward rupture directivity, the pulses associated with the main phases become sharper enhancing the amplitude of high frequency phases.

Figure 20b shows the results of simulations for the 3D model with scattering. Scattering increases the time duration of the directivity pulse and reduces the high frequency energy of the signal at all stations. Although effective in reducing the high frequency energy at all receivers, the wave scattering does not completely destroy the high frequency effects of rupture directivity. This is clearly shown in Figure 21 where we compare the amplitude Fourier spectra of the signal recorded at station 12 (forward rupture directivity) and station 4 (backward rupture directivity) for the 1D model and 3D-scattering model. In this figure we can clearly see that scattering reduces the amplitude of high frequency motion, but it does not modify the rupture directivity effects of rupture propagation which is expressed by the difference in waveform between motions at stations located in the rupture propagation direction (station 12), and opposite to the rupture propagation direction (station 4). This result demonstrates that in general, the rupture directivity effect expressed in azimuthal changes of the S wave amplitude due to rupture propagation is not affected by wave scattering. Instead it remains visible in a broad frequency range as shown by Tan and Helmberger (2009).

9. Scattering Effects

Empirical data from earthquakes and explosions have revealed that ground motions from explosions contain a considerable amount of S wave energy (e.g., Walter *et al.*, 1995; Walter and Taylor, 2002; Saikia, 1992; Saikia *et al*, 2001). Theoretically, we expect S-waves from explosions to be weak at all frequencies since they can only come from pS waves, assuming the

usual simple 1D modeling. Since the surface generally has low velocities, this conversion of wave-types is small, therefore a flat free-surface has a small contribution to S wave energy. It is important to know how some explosions generate shear wave energy. Some explosions are best modeled with CLVD's (e.g., Patton, 2007), suggesting that S wave energy is generated at the source. Near-in data suggests such contributions as well, Saikia (2006).

Recent investigation of factors that affect the spectral content of S waves during explosions based on analyses of recorded data and two-dimensional numerical modeling suggest that a large portion of the S waves is created as a result of P to S wave conversion at the free surface as well as wave scattering in the source region (e.g., Mc Laughlin *et al.*, 1986). Due to complexities in the surface structure, including topography and micro-basins, the free-surface reflection coefficients for different waves become complex. Because of wave interference, the frequency content of the primary waves is altered, thus leading to modifications in the spectrum of the source-originated P and S waves. This means that the observed P/S spectral ratio depends not only on the source type but also on surface and underground complexities of the medium surrounding the source. It is therefore very important to understand and quantify the effects of interaction between primary waves with the source-emplacement structural complexities during explosions.

In order to study waveform differences between earthquakes and explosions, we extend the frequency range of our 3D modeling to higher frequencies by performing numerical simulations of wave scattering using a regional 3D velocity model of the crust with flat topography. The exclusion of topography allows the calculation of full waveforms at regional distances up to 350km and frequencies up to 3.5Hz. All simulations were performed on the computer cluster at Caltech using 300 – 400 nodes. We calculated full seismograms using a double couple point source at 2km depth with an arbitrary focal mechanism, and an isotropic explosion point source at a depth of 500m. Figure 22 shows a map view of the crustal velocity model used in our simulations. The crustal 3D velocity model includes flat layers and large scale and small-scale structural heterogeneities.

The comparison between the earthquake source and explosion is shown in Figure 23. In this figure we compared vertical component seismograms calculated at a linear array of stations shown in Figure 22, band pass filtered at 0.1-3.5Hz and 2.0-3.6Hz. All synthetic seismograms are scaled to unit maximum amplitude in order to facilitate the comparison between P, S and Lg coda waves in each seismogram. As in previous models with surface topography, the generation of secondary S waves and S and Lg coda waves for the isotropic explosion source is impressive. The wave propagation scattering can produce Lg, P and S coda waves with significant energy even for isotropic explosion sources. Other simulations performed with the same scattering model confirm that the energy of Lg coda waves increases when the source depth decreases. An even more drastic effect was seen for the P coda waves. The explosion waveforms are dominated by high frequency P coda waves and low frequency Lg coda waves (Figure 23a).

At high frequencies the relative energy of P and Lg waves starts to show significant differences between the explosion and earthquake (Figure 23b). The P/L ratio is much larger for the explosion. The difference in P/Lg ratio between the explosion and earthquake at high frequency is controlled more by P rather than Lg waves. As demonstrated by our simulation, the energy of

Lg coda waves for both explosion and deep earthquake sources are very similar. At longer distances, P waves generated by the explosion become richer in high frequency energy compared with the P waves coming from the earthquake source (see Figure 23a). This is probably due to the fact that for shallow sources P and converted P to S waves remain trapped within the scattering structure of the shallow crust. In contrast, P waves coming from a deeper source, besides being attenuated, do not develop much coda wave amplitude as some of the energy reflected at the free surface leaks back to the deeper crust.

Another interesting characteristic of P waves is the P(high.freq.)/P(low.freq.) ratio. Our simulations suggest that P(high.freq.)/P(low.freq.) for the explosion is different from that of the earthquake. Using the simulated waveforms we estimated the P(2-3.5Hz)/P(0.1-1.0Hz) and P(2-3.5Hz)/Lg(2-3.5Hz) ratios at 95 sites. The time window used for the P wave includes the direct P and P coda waves. The comparison of these ratios between the explosion and earthquake is shown in Figure 24. Our result shows that for structures with shallow wave-path scattering P(high.freq.)/P(low.freq.) ratio is different between earthquakes and explosions at short distances, but more similar at larger distances. In contrast, the P/Lg ratio at high frequencies shows differences at larger distances. The vertical component is more affected by the 3D wave propagation scattering and free surface topography.

Our numerical experiments with 3D velocity models that include random velocity perturbations and microbasins, representing wave scattering in the upper 5km of the crust, clearly show that wave-path scattering is a major contributor to S and Lg coda waves from explosions. The energy of Lg coda waves depends on the source depth.

10. Conclusions

The source radiation pattern of P waves can be observed at frequencies as high as 8Hz.

P-S conversions contribute to a significant increase in amplitude of P coda waves in the tangential component at high frequencies.

S waves are more susceptible to wave propagation scattering than P waves. The radiation pattern effect of S waves is largely distorted at frequencies above 2Hz. At these frequencies the amplitude of all three components becomes similar. This suggests that at high frequencies the amplitude of S wave coda does not follow the source radiation pattern. At high frequencies the S wave radiation pattern is mainly controlled by wave scattering in the crust. This very robust feature of S coda waves could be used to derive stable estimates of source parameters.

The comparison of waveform envelopes between an earthquake and North Korean explosion shows that on long wave paths, the P/S ratios between the earthquake and explosion are very different due to wave scattering. The P/S ratio for the explosion at MDJ is much larger. These observations suggest that at large epicentral distances, the cumulative effect of wave scattering on the P/S coda wave ratio is enhanced. This observation is very well reproduced by our simulations of 3D wave scattering.

Near-source wave scattering has important implications for shaping the source energy radiation at local and teleseismic distances. It also affects the amplitude of depth phases. The analyses of the Big Bear earthquake sequence by Tan and Helmberger (2009) and results of our simulations of fault zone trapped waves demonstrate that wave propagation scattering in the fault damage zone causes very complex waveforms. The small-scale heterogeneities affect the S waves more than the P waves which have longer wavelengths. We infer that this feature is caused by fault-zone damage where energy is locally trapped in the slow leaky waveguide and then re-radiated from the lateral edges of the fault zone. Our 3D numerical simulation demonstrates the implication of fault zone damage on observed waveform scattering of P and S waves.

We have examined the combined effects of wave propagation scattering due to complexities in the shallow crust and surface topography in relation to the source depth. Our simulation result suggests that high frequency scattering is more stable than low frequency scattering under changes in source depth. The slope of the high frequency envelope does not depend on the source depth. In contrast the slope of the low frequency envelope depends on the source depth.
We performed several numerical experiments to assess the effects of near-source structure, including micro-basins, surface topography, and small-scale shallow heterogeneities on local and teleseismic waveforms. Our simulation demonstrates that the amplitude of P and S coda waves for shallow sources is sensitive to the structural complexities near the source. For sources located inside the basin and near the basin edge, scattering due to basin edge effects reduces the amplitude of P coda waves while it increases the amplitude of S coda waves. This is in contrast to the situation for sources outside the basin.

Our simulations of fault zone damage effects suggest that when the earthquake is located within the fault zone the S wave pulse duration increases. Therefore S waves perturbed by the fault zone structure may not directly reflect information about the source rupture process. They tend to be contaminated by wave scattering which largely depends on the relative location of the earthquake with respect to the fault zone. Also our simulations suggest that the amplitude of coda waves from earthquakes located near or in the fault zone depends on the fault zone orientation and whether the fault zone reaches the free surface. Buried fault zones may not generate strong surface waves.

Scattering reduces the amplitude of high frequency motion, but it does not modify the rupture directivity effects of rupture propagation, which is expressed as a difference in waveform between motions at stations located in the forward and backward rupture propagation directions. This result demonstrates that in general, the rupture directivity effect is expressed by azimuthal changes in S wave amplitude due to rupture propagation, and is not affected by wave scattering. Instead it remains visible in a broad frequency range as shown by Tan and Helmberger (2009).

Our simulation of shallow earthquakes and explosions suggests that the amplitude ratio between P and Rg coda waves is still higher for the explosion source at high frequencies. Our simulations clearly show that because S coda waves have shorter wavelength, their amplitude diminishes faster than that of P coda waves at long distances. This result is in agreement with similar observations made when we compared the North Korean explosion and a nearby earthquake at short and regional distances. P coda waves from the explosion have relatively large amplitudes compared to P coda waves from the earthquake. The cumulative effect of scattering caused by

the surface topography and spatial structural heterogeneities contribute to generation of P coda waves through P/S and S/P conversions. At high frequencies the difference of P/Rg ratio between the explosion and the earthquake source is significant, unlike the case for low frequencies.

Our numerical experiments with 3D velocity models that include random velocity perturbations and microbasins, representing wave scattering in the upper 5km of the crust, clearly show that wave-path scattering is a major contributor to S and Lg coda waves from explosions and shallow earthquakes. The energy of Lg coda waves depends on the source depth. P/Lg ratios below 1Hz and short distances are very similar for shallow explosions and deeper earthquakes.

References

Aki, K. (1969). Analysis of the seismic coda of local earthquakes as scattered waves, *J. Geophys. Res*., 74, 615-631.

Aki, K. and B. Chouet (1975). Origin of coda waves: source, attenuation and scattering effects, *J. Geophys. Res*. 80, 3322-3342.

Ben-Zion, Y. (1998). Properties of seismic fault zone waves and their utility for imaging low velocity structures, *J. Geophys. Res*., 10, 1257-12585.

Ben-Zion, Y., Z. Peng, M.A. Lewis, J. McGuire (2007). High resolution imaging of fault zone structures with seismic fault zone waves, Scientific Drilling, Special Issue No.1,78-79.

Dainty, A.M. (1984). High frequency acoustic backscattering and seismic attenuation, *J. Geophys. Res*., 89(B5), 3172-3176.

Dainty, A. (1996). The influence of seismic scattering on monitoring. *Monitoring a Comprehensive Test Ban Treaty. E.S. Husebye and A.M. Dainty (Editors*), 663-688.

Day, S. and McLaughlin, K.L. (1991). Seismic source representations for spall. *Bull. Seism. Soc. Am.*, 81,191-201.

Day, S.M. and C.R. Bradley (2001). Memory-efficient simulation of anelastic wave propagation, *Bull. Seism. Soc. Am*., 91(3), 520-531.

Frankel, A. and J. Vidale (1992). A three-dimensional simulation of seismic waves in the Santa Clara Valley, California, from a Loma Prieta aftershock, *Bull. Seism. Soc. Am.* 82**,** 2045-2074.

Frankel, A. and R.W. Clayton (1986). Finite difference simulations of seismic scattering: implications for the propagation of short-period seismic waves in the crust and models of crustal heterogeneity, *J. Geophys. Res*., 91(B6), 6465-6489.

Frankel, A. and L. Wennerberg (1987). Energy-flux model of seismic coda: Separation of scattering and intrinsic attenuation, *Bull. Seism. Soc. Am*., 77(4), 1223-1251.

Graves, R.W., A. Pitarka, and P.G. Somerville (1998). Ground motion amplification in the Santa Monica area: effects of shallow basin edge structure, *Bull. Seism. Soc. Am*., 88, 881-897.

Graves, R., and A. Pitarka (2004). Broadband time history simulation using a hybrid approach, *Proceeding 13th World Conference on Earthquake Engineering*, Vancouver, B. C., Canada, Paper #1098.

Graves, R. and S. Day (2003). Stability and accuracy of the coarse-grain viscoelastic simulation, *Bull. Seism. Soc. Am*., 93, 283-300.

Gupta, I.N., and R.R. Blandford (1987). A study of P-waves from Nevada test site explosions: near-source information from teleseismic observations?, *Bull. Seism. Soc. Am*., 77, 1041-1056.

Hartzell, S., S. Harmsen, A Frankel, and S. Larsen (1999). Calculation of broadband time histories of ground motion: comparison of methods and validation using strong ground motion from the 1994 Northridge earthquake, *Bull. Seism. Soc. Am*., 89, 1484-1504.

He, Y. X., Xie, and T. Lay (2008). Explosion-source energy partitioning and Lg-wave excitation: Contributions of free-surface scattering, *Bull. Seism. Soc. Am*., 98, 778-792.

Kim, W. and P.G. Richards (2007). North Korean Nuclear Test: Seismic Discrimination at Low Yield, *Transactions American Geophysical Union*, Volume 88, Issue 14, p. 158-161.

Langston, C.A. (1989). Scattering of teleseismic body waves under Pasadena, California, *J. Geophys. Res*., 94, 1935-1951.

Lay, T. (1991). The teleseismic manifestation of pP: Problems and paradoxes, in: *Explosion Source Phenomenology*, AGU Geophysical Monograph 65, (S. Taylor, H. Patton, P. Richards, eds.), 109-125.

Lay, T., L.J. Burdick, and D.V. Helmberger (1984). Estimating the yields of the Amchitka tests by waveform intercorrelation. *Geophys. J. Intl*. 78, 181-207.

Lay, T. and J. Welc (1987). Analysis of near-source contributions to early *P*-wave coda for underground explosions. 1. Waveform complexity, *Bull. Seism. Soc. Am.*, 77, 1017-1040.

Liu, P., R. Archuleta, and S. Hartzell (2006). Prediction of broad-band ground motion time histories: Hybrid low/high frequency method with correlated random source parameters, *Bull. Seism. Soc. Am.*, 97, 2118-2130

Mayeda K. M., A. Hofstetter, J.L. O'Boyle and W.R. Walter (2003). Stable and transportable regional magnitudes based on coda-derived moment rate spectra, *Bull. Seism. Soc. Am*., 93, 224-239.

McLaughlin, K.L., L.M. Anderson, and A.C. Lees (1986). Effects of local geologic structure for Yucca Flats, NTS, explosion waveforms: 2-dimensional linear finite difference simulations, *Tech. Report AFGL-TR-86-0220*, Geophysics Lab, Hanscom AFB, MA.

McLaughlin, K.L. Stevens, J.L. Barker, T.G. Day, S.M. and Skoller, B, (1993). 2D and 3D numerical modeling of seismic waves from explosion sources, *Computers in Physics*.

Mitchell, B.J., J. Xie, and Y. Pan (1995). Attenuation and blockage of Lg in Eurasia, in *Monitoring a Comprehensive Test Ban Treaty*, Edited by E.S. Husebye and A.M. Dainty, Kluwer Academic Publishers, Boston, 645-654.

Myers, S., J. Wagoner, S. Larsen, A. Rodgers, K. Mayeda, K. Smith, and W. Walter (2003). Simulation of regional explosion S-phases (SiRES) Project, *Proceedings of the 25th SRR – Nuclear Explosion Monitoring, Building Knowledge Base, Vol I NNSA*, 117-124, Tucson, Arizona.

Myers, S.C., J. Wagoner, S. Larsen, L. Preston and K. Smith (2005). The effect of topography and near-source geologic heterogeneity on the generation of short-period explosion S waves, *Abstract at Annual SSA meeting at Lake Tahoe*, 223p.

Ni, J. and Barazangi, M. (1983). High frequency seismic wave propagation beneath the Indian shield, Himalayan Arc, Tibetan Plateau, and surrounding regions: high uppermost mantle velocities and efficient Sn propagation beneath Tibet, *Geophys. Jour. Roy. Astron. Soc*. 72, 655-689.

Patton, H.J, and S.R. Taylor (1995). Analyses of Lg spectral ratios from NTS explosions: implications for the source mechanisms of spall and generation of *Lg* waves, *Bull. Seism. Soc. Am*., 85, No. 1, 220-236.

Patton, H. (2007). Next Generation Explosion Source Model, *Seism. Res. Lett.*, 78, No. 2, 241.

Phillips, W.S., H.E. Hartse, S.R. Taylor and G.E. Randall (2000). 1 Hz Lg Q tomography in central Asia, *Geophys. Res. Lett*., 27, 3425-3428.

Pitarka, A., K. Irikura, T. Iwata, and H. Sekiguchi (1998). Three-dimensional simulation for the near-fault ground motion for the 1995 Hyogo-Ken Nanbu (Kobe), Japan earthquake, *Bull. Seism. Soc. Am*., 88, 428-440.

Pitarka, A. (1999). 3D elastic finite-difference modeling of seismic motion using staggered grid with nonuniform spacing, *Bull. Seism. Soc. Am*., 89, 54-68.

Pitarka, A. and L. Dalguer (2003). Estimation of dynamic stress parameters of the 1992 Landers earthquake, *Abstract, AGU Fall Meeting*, San Francisco.

Pitarka, A., P.G. Somerville, Y. Fukushima, T. Uetake, K. Irikura (2000). Simulation of near-fault ground motion using hybrid Green's functions, *Bull. Seism. Soc. Am*., 90, 566-586.

Pitarka, A. and K. Irikura (1996a). Basin structure effects on long-period strong motions in the San Fernando valley and Los Angeles basin from the 1994 Northridge earthquake and an aftershock, *Bull. Seism. Soc. Am*, 86, 1B, S126-S137.

Pitarka, A and K. Irikura (1996b). Modeling 3D surface topography by finite-difference method: Kobe-JMA station site, Japan case study, *Geophys. Res. Lett*., 20, 2729-2732.

Pitarka, A., D. Helmberger, and S. Ni (2008). Analyses and simulation of 3D scattering due to heterogeneous structure and surface topography on regional phases; magnitude discrimination, *Proceedings of the 30th Seismic Research Review: Ground –Motion Based Nuclear Explosion Monitoring Technologies, Vol I NNSA.*

Rodgers, A. and J. Tromp (2005). Modeling nuclear explosions and earthquakes using spectral element method and high-performance computing, *Abstract, Annual SSA meeting at Lake Tahoe*, 223p.

Saikia C. (1992). Numerical study of quarry generated Rg as a discriminant for earthquakes and explosions: Modeling of Rg in Southwestern New England, *J. Geophys. Res*., 97, 11057-11072.

Saikia, C.K. (1994). Modified frequency-wave-number algorithm for regional seismograms using Filon's quadrature-modeling of L(g) waves in eastern North America, *Geophys. J. Int., 118*, 142-158.

Saikia, C.K., D.V. Helmberger, R.J. Stead and B.B. Woods (2001). Effects of source RDP models and near-source propagation: implication for seismic yield estimation, *Pure and Applied Geophys*., 158, 2173-2216.

Saikia, C.K. (2006). Modeling of the 21 May 1997 Jabalpur earthquake in central India: Source parameters and regional path calibration, *Bull. Seism. Soc. Am*., 96, No. 4A, 1396-1421.

Saito, T., H. Sato, M. Fehler, and M. Ohtake (2003). Simulating the envelope of scalar waves in 2D random media having power-law spectra of velocity fluctuation, *Bull. Seism. Soc. Am*., 93(1), 240-252, 2003.

Stead, R.J. (1989). Finite differences and a coupled analytical technique with applications to explosions and earthquakes, *Ph.D. Dissertation*, California Institute of Technology, Pasadena, CA, p337.

Stead, R. and D. Helmberger (1988). Numerical-analytical interfacing in two-dimensions with applications to modeling NTS seismograms, *Pure and Applied Geophys.*,128,159-174.

Stevens, J.L., G.E. Baker, H, Xu, T. Bennet, N. River, S.M. Day (2003). The physical basis of Lg generation by explosion sources, *Proceedings of the 25th SRR – Nuclear Explosion Monitoring, Building Knowledge Base, Vol I NNSA*, 456-465, Tucson, Arizona.

Takenaka, H. B.L.N. Kennett, and H. Fujiwara (1996). Effect of 2-D topography and 3-D seismic wavefield using a 2.5-D discrete wavenumber-boundary integral equation method, *Geophys. J. Int*., 124, 741-755.

Tan, Y., L. Zhu, D.V. Helmberger, and C.K. Saikia (2006). Locating and modeling regional earthquakes with two stations, *J. Geophys. Res*., 111, B01306, doi:10.1029/2005JB003775.

Tan, Y. and D.V. Helmberger (2009). Rupture directivity of the Big Bar earthquake sequence, *Bull. Seism. Soc. Am*. (submitted)

Walter, W., K.M. Mayeda, and H.W. Patton (1995). Phase and spectral ratio discriminants between NTS earthquakes and explosions. Part I: Empirical observations, *Bull. Seism. Soc. Am*., 8, 1050-1067.

Walter, W.R. and. S.R. Taylor (2002). A revised magnitude and distance amplitude correction (MDAC) procedure for regional discriminants: Theory and testing NTS., *Los Alamos National Laboratory, LA-UR-02-1008*, 15pp.

Wu, Ru-Shan, S. Jin, and Xiao-Bi Xie (2000). Seismic wave propagation and scattering in heterogeneous crustal waveguides using screen propagators: I SH-waves, *Bull. Seism. Soc. Am.*, 90, 401-413.

Xie, X., T. Lay, and R. Wu (2005). Near-source energy partitioning for regional waves in 2D and 3D models, contributions of S^*-to-Lg and P-to-Lg scattering, *Proceedings of the 27th Seismic Research review: Ground –Motion Based Nuclear Explosion Monitoring Technologies, Vol I NNSA*, 249-258.

Zeng Y., J.G. Anderson, and F. Su (1995). Subevent rake and random scattering effects in realistic strong ground motion simulation, *Geophys. Res. Lett*., 22(1), 17-20.

Zeng, Y., J.G. Anderson, and G. Yu (1994). A composite source model for computing realistic synthetic strong ground motions, *Geophys. Res. Lett*., 21(8), 725-728.

Zeng, Y. (1993). Theory of scattered P- and S-wave energy in a random isotropic scattering medium, *Bull. Seism. Soc. Am*., 83(4), 1264-1276.

Zeng, Y. F. Su, and K. Aki (1991). Scattering wave energy propagation in random isotropic scattering medium 1.Theory, *J. Geophys. Res*., 96(B1), 607-619.

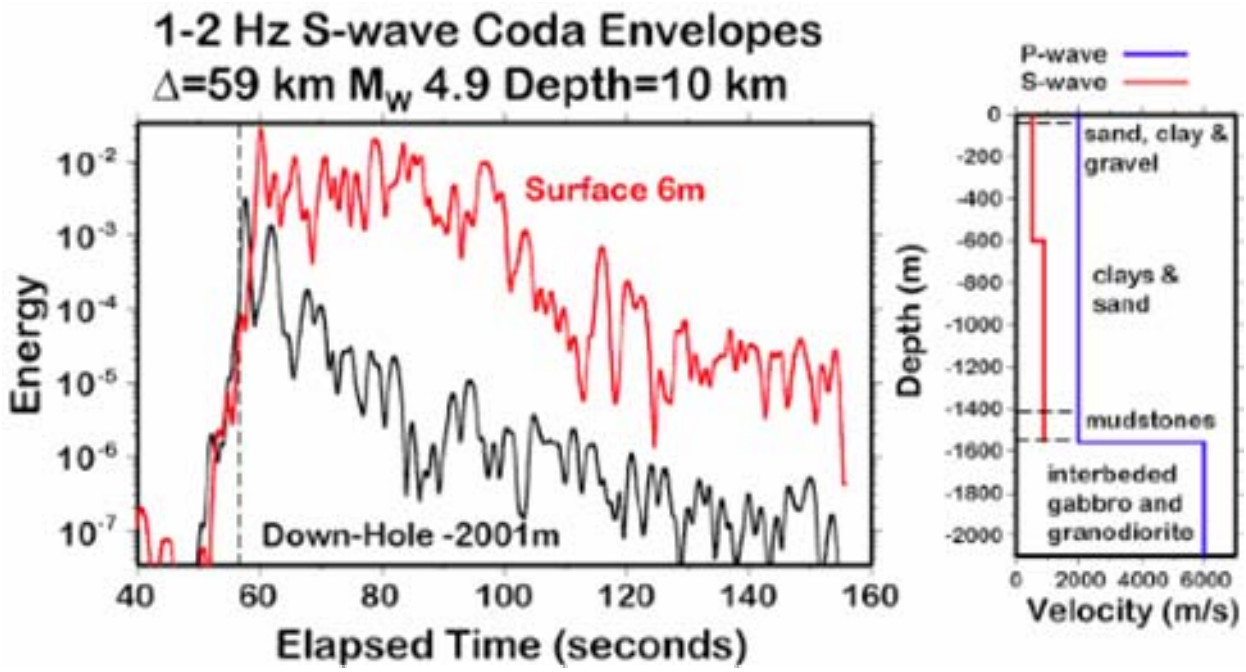

Figure1. Comparison of S-wave coda energy envelopes between down- and up-hole KiKnet seismometers placed at the surface elevation of 6 m and a depth of 2001 m. The site is in the Osaka region of Japan and is characterized as a 1600 m thick sedimentary basin over granite rock. The surface recording shows significant scattering for approximately 40 sec duration within the sedimentary basin relative to the 2001 m deep borehole recording below the basin in granite bedrock. We corrected the surface recording by a factor of 2 for the free surface amplification but did not account for the amplification due to the impedance contrast between rock and soil.

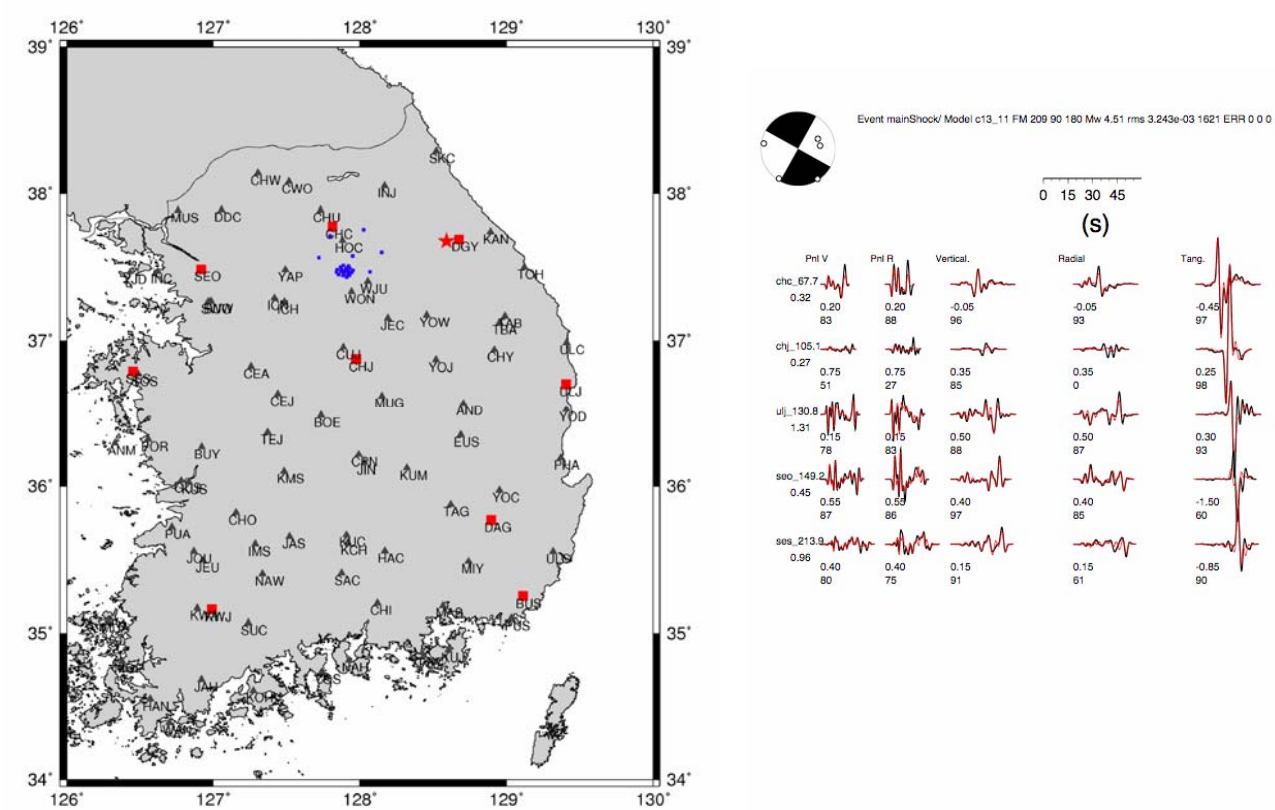

Figure 2. (Left panel) Map showing broad-band (red square) and short-period strong motion (black triangle) stations in South Korea. Blue squares show IMS (KSRS) stations, and the red star indicates the epicenter of the Mw 4.5 070120 earthquake analyzed in this study. (Right panel) Focal mechanism of the earthquake and waveform fit obtained with a cut and paste (CAP) inversion technique.

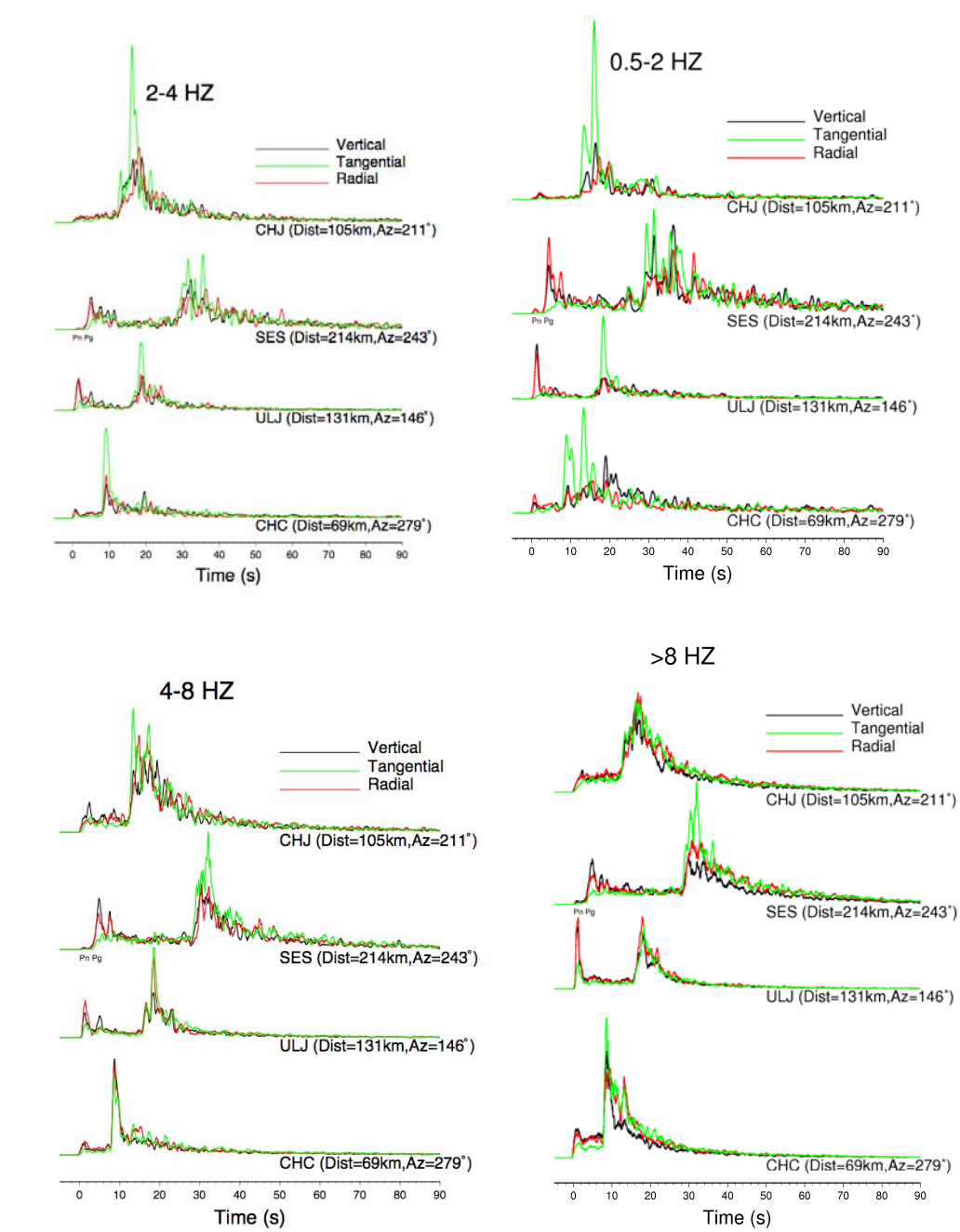

Figure 3. Smoothed envelopes of broad-band velocity seismograms recorded at station CHJ, SES, ULJ, and CHC from the Mw 4.5 070120 earthquake in South Korea. The envelopes are calculated at four frequency bands indicated on top of each panel. Note the large amplitude of the P wave on the vertical and radial components at stations CHJ, SES and ULJ which are located near nodal planes. The difference in the P wave seen between the three components caused by the source radiation is preserved only at frequencies up to 4 Hz. In general, at frequencies higher than 4 Hz, the amplitude of P wave coda become similar on all components. This is a clear indication of scattering effects in the shallow crust.

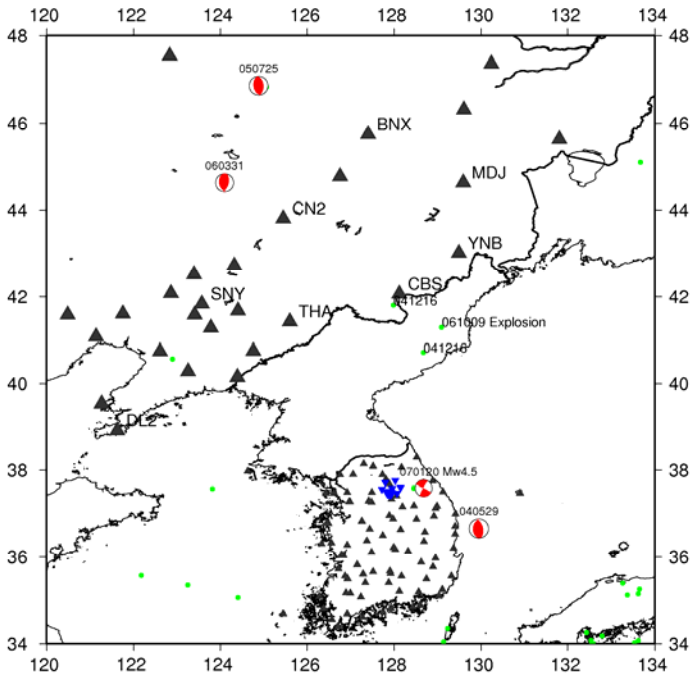

Figure 4. Map of southeastern China and Korean Peninsula. Triangles indicate broadband and short period stations of the China Seismic Network and Korean Seismic Network. The 061009 explosion and 020416 earthquake located in the Korean peninsula, analyzed in this study, are shown by green dots.

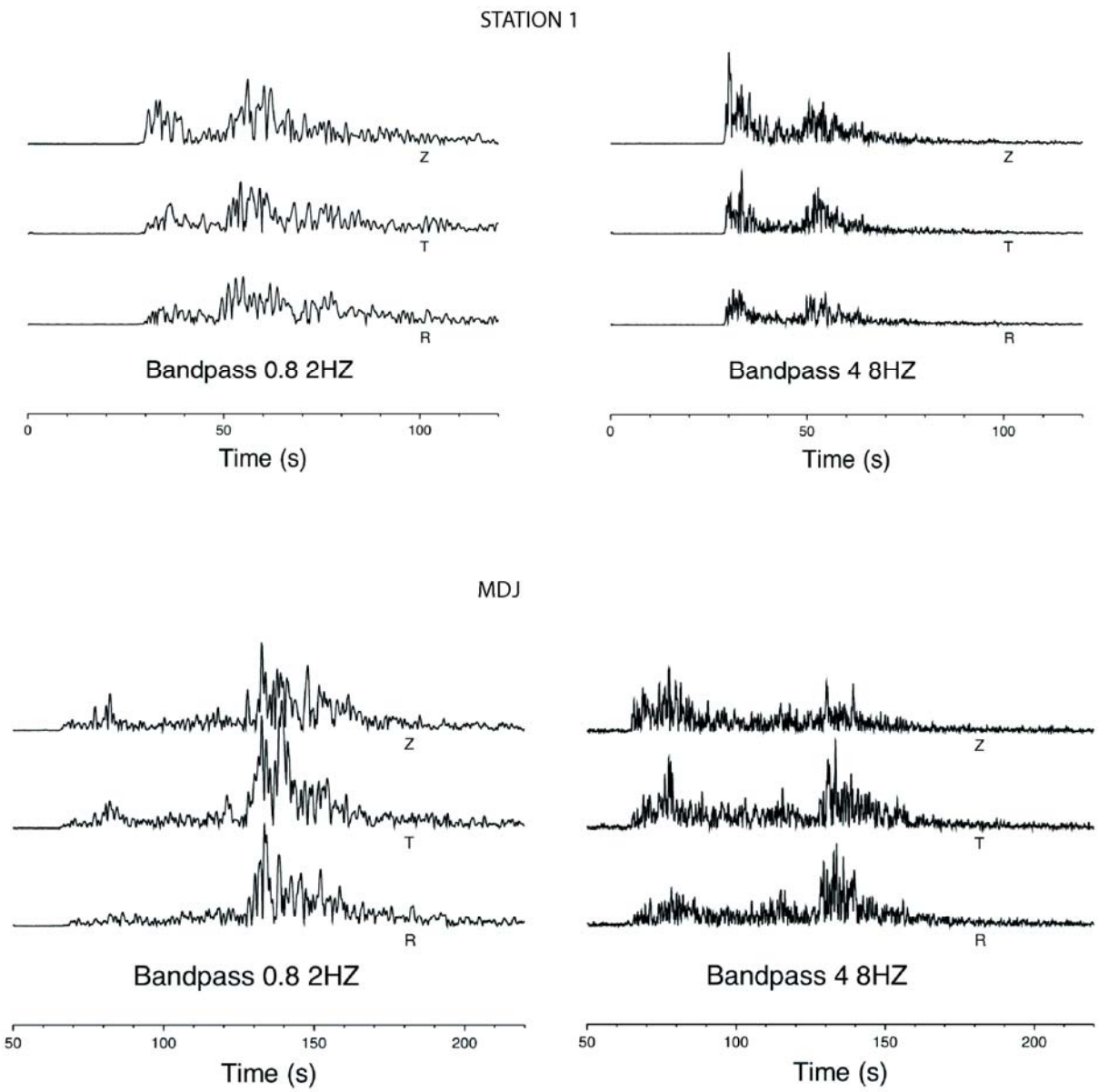

Figure 5a. Smoothed envelopes of velocity seismograms from the 020416 earthquake in North Korea recorded at STATION 1 (top panels) and MDJ (bottom panels) in the frequency ranges 0.8-2 Hz and 4-8 Hz.

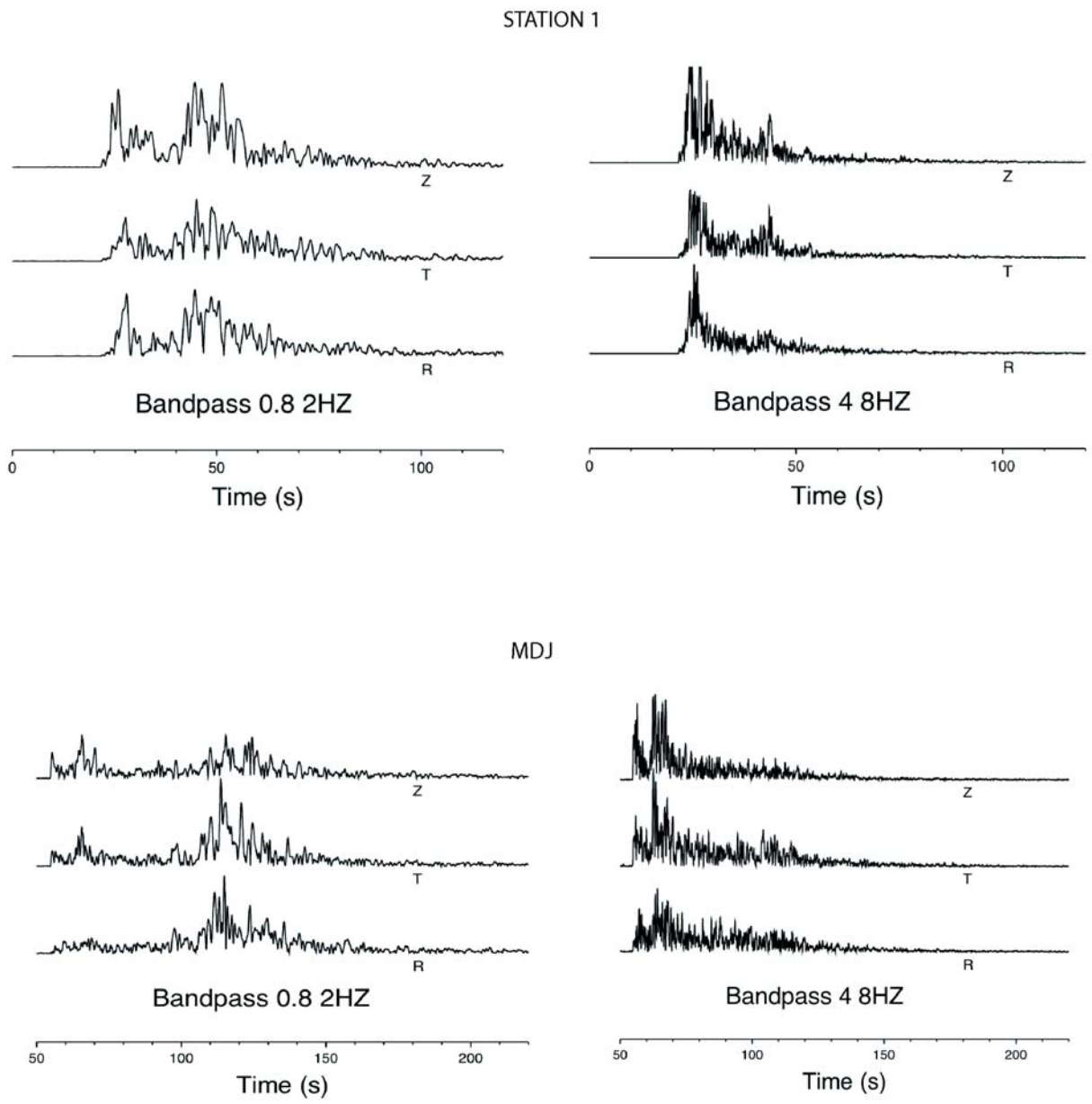

Figure 5b. Smoothed envelopes of velocity seismograms from the 061009 North Korean explosion recorded at STATION 1 (top panels) and MDJ (bottom panels) in the frequency ranges 0.8-2 Hz and 4-8 Hz.

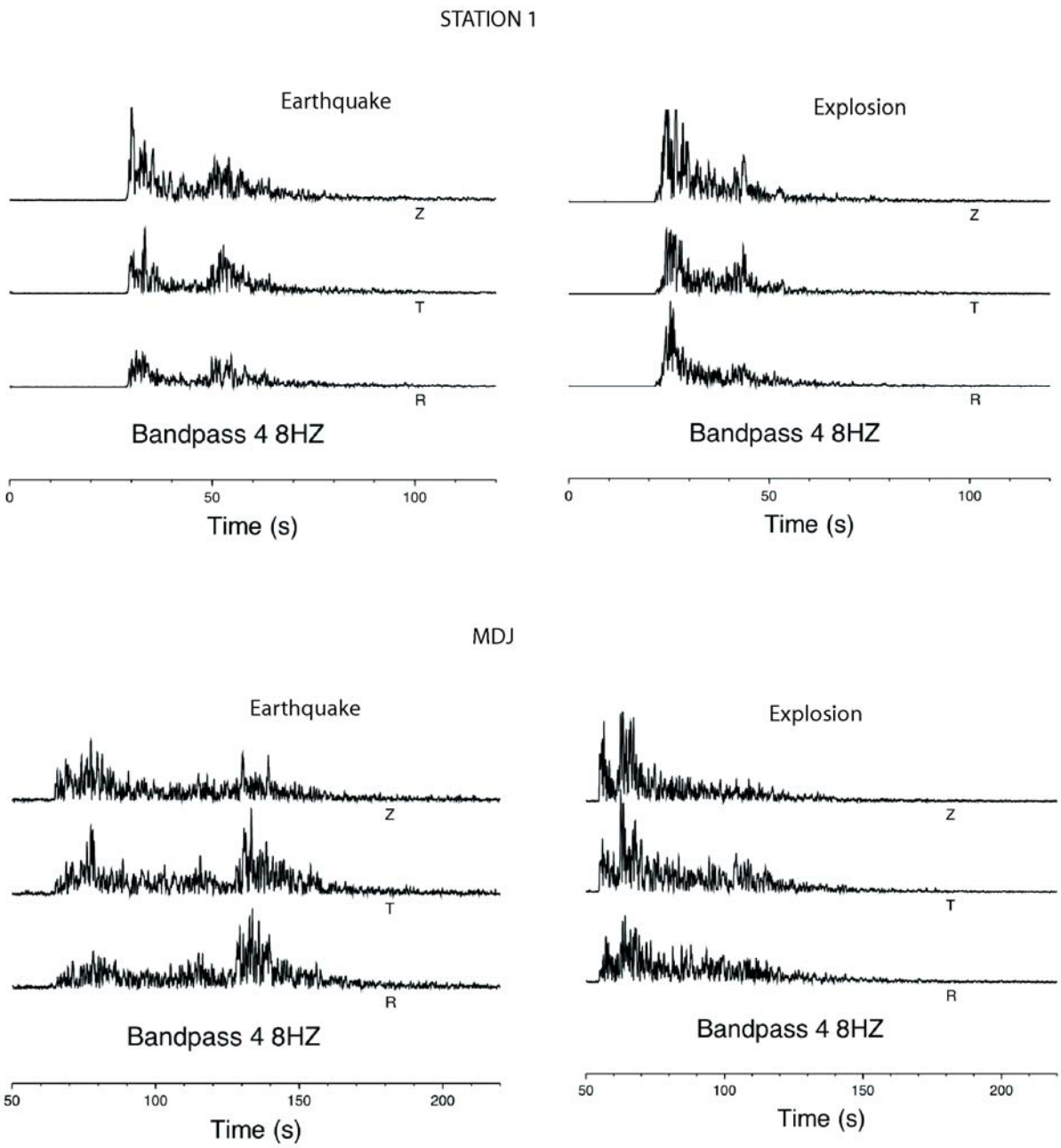

Figure 5c. Comparison of smoothed envelopes of velocity seismograms at STATION1 and MDJ from the 020416 earthquake (left panels) and 061009 explosion (right panels) in North Korea band-pass filtered at 4-8 Hz.

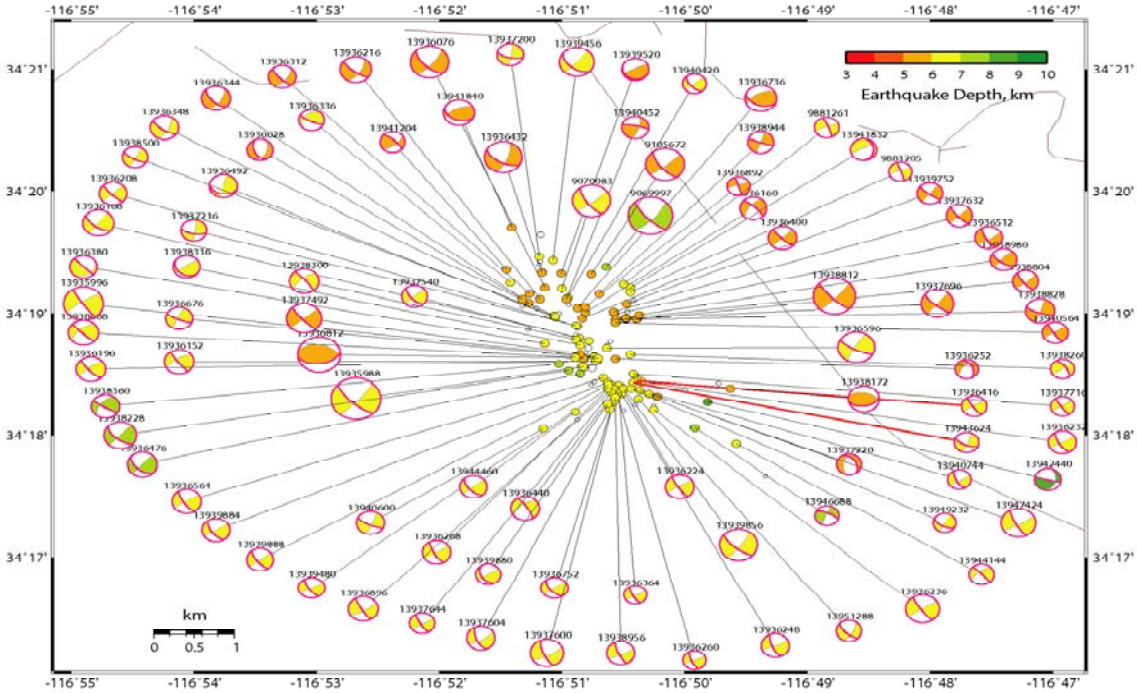

Figure 6. Focal mechanisms of the Big Bear earthquake sequence (Tan and Helmberger, 2009)

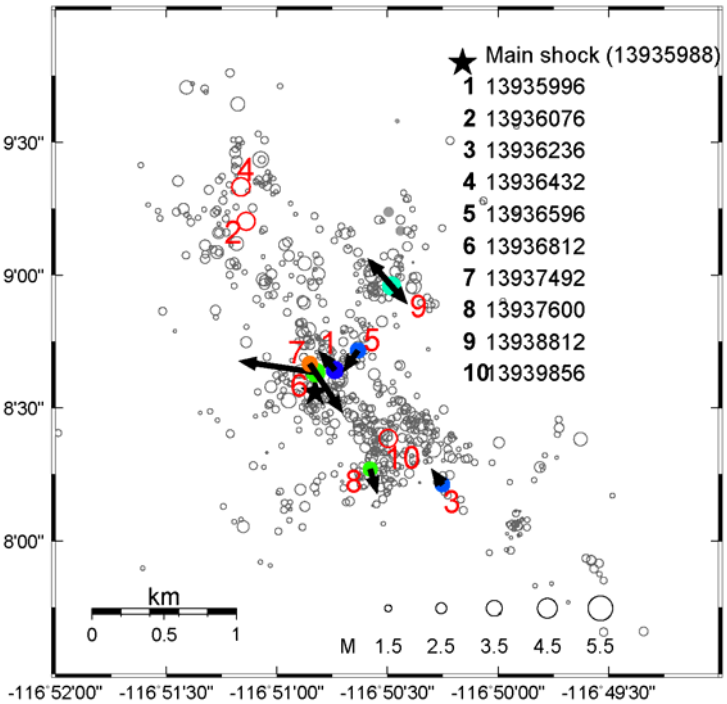

Figure 7. Inferred rupture directivity (arrows) for selected events and relocated seismicity from Chi and Hauksson (2006). The events with reliable rupture parameters are color coded depending on the estimated stress drop. The arrow points to the rupture direction while their length is proportional to the estimated fault length. The rupture planes have complex orientations indicating complex faulting.

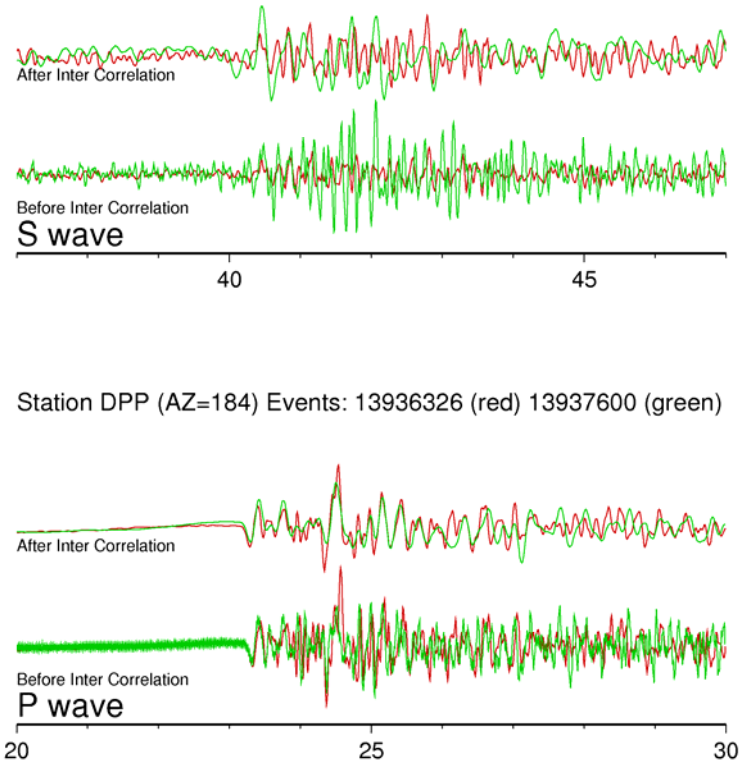

Figure 8. Intercorrelations between recordings of two small events at DPP using S waves (top panel) and P wave (bottom panel). The better intercorrelation for P waves indicates that P waves are less affected by wave scattering in the fault zone.

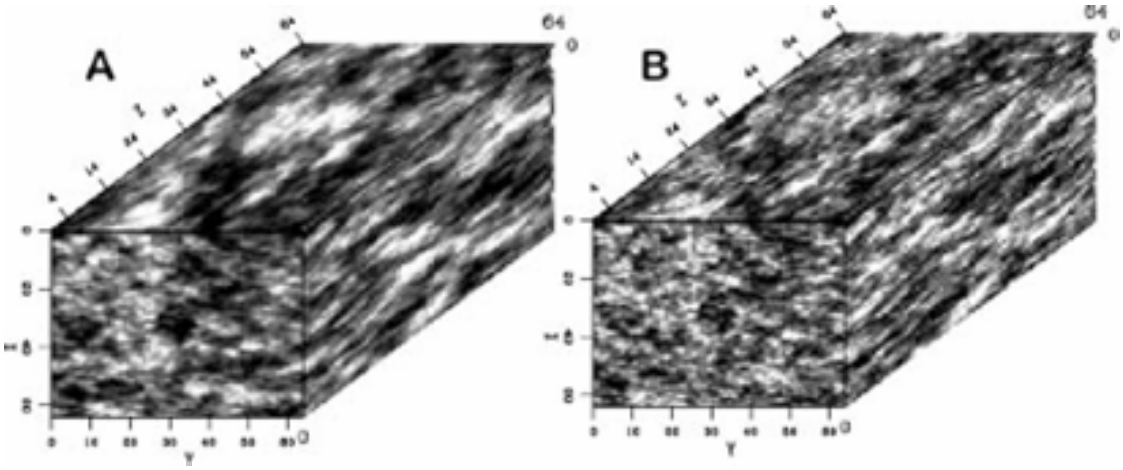

Figure 9. Three-dimensional media with random velocity variations based on exponential (A) and von Karman functions (B).

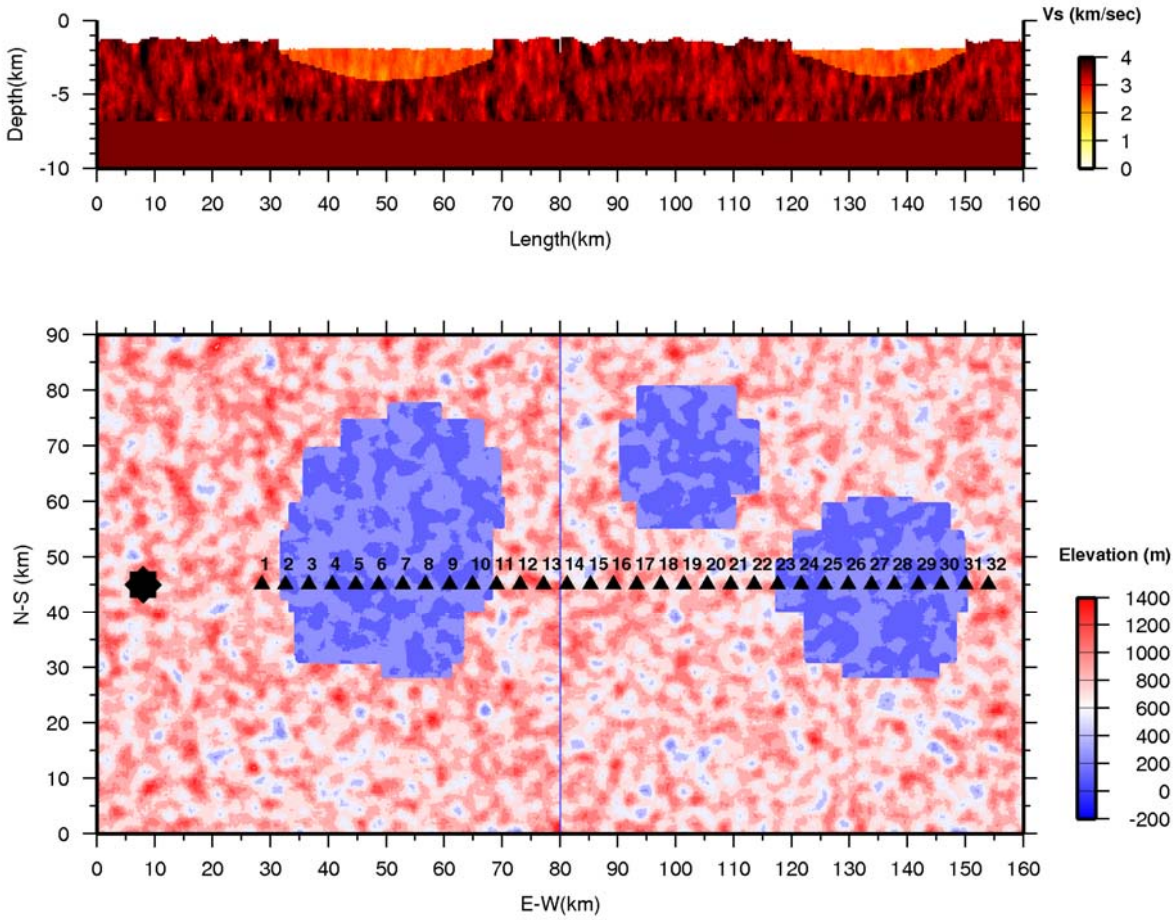

Figure 10. Velocity model with smooth topography used in simulations of wave propagation scattering. Top Panel: Cross-section of the top 7 km of the velocity model along the source-station linear array. The velocity is randomly perturbation in the upper 5 km of the crust. The maximum elevation is 1400m with a correlation of 3 km. The maximum velocity perturbation is 10% and the correlation length of perturbations is 1.5 km. There is a factor of 3 vertical exaggeration. Bottom Panel: Topographic elevation. Triangles indicate stations, and star indicates the epicenter location.

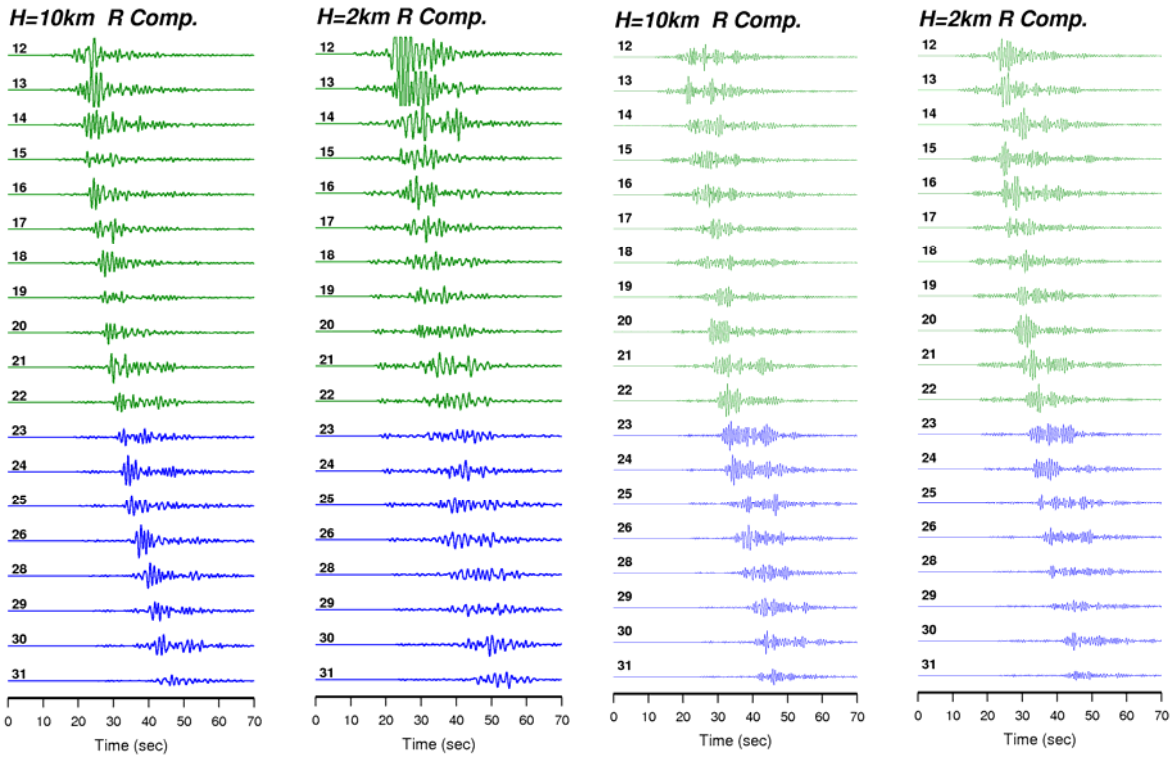

Figure 11. Vertical component of synthetic velocity for a strike-slip double-couple point source located at depths of 10 km (left panel) and 2 km (right panel). The synthetic seismograms are calculated with a 3D model that includes shallow crustal scattering effects (shown in Figure 10). The synthetics are band-pass filtered at 0.1-1.0 Hz. (two left panels), and at 1.0-1.8 Hz. (two right panels). There is little difference at the higher frequencies. This suggests that high frequency scattering is more stable than the low frequency scattering caused by microstructure. Green traces correspond to rock sites, and blue traces correspond to basin sites.

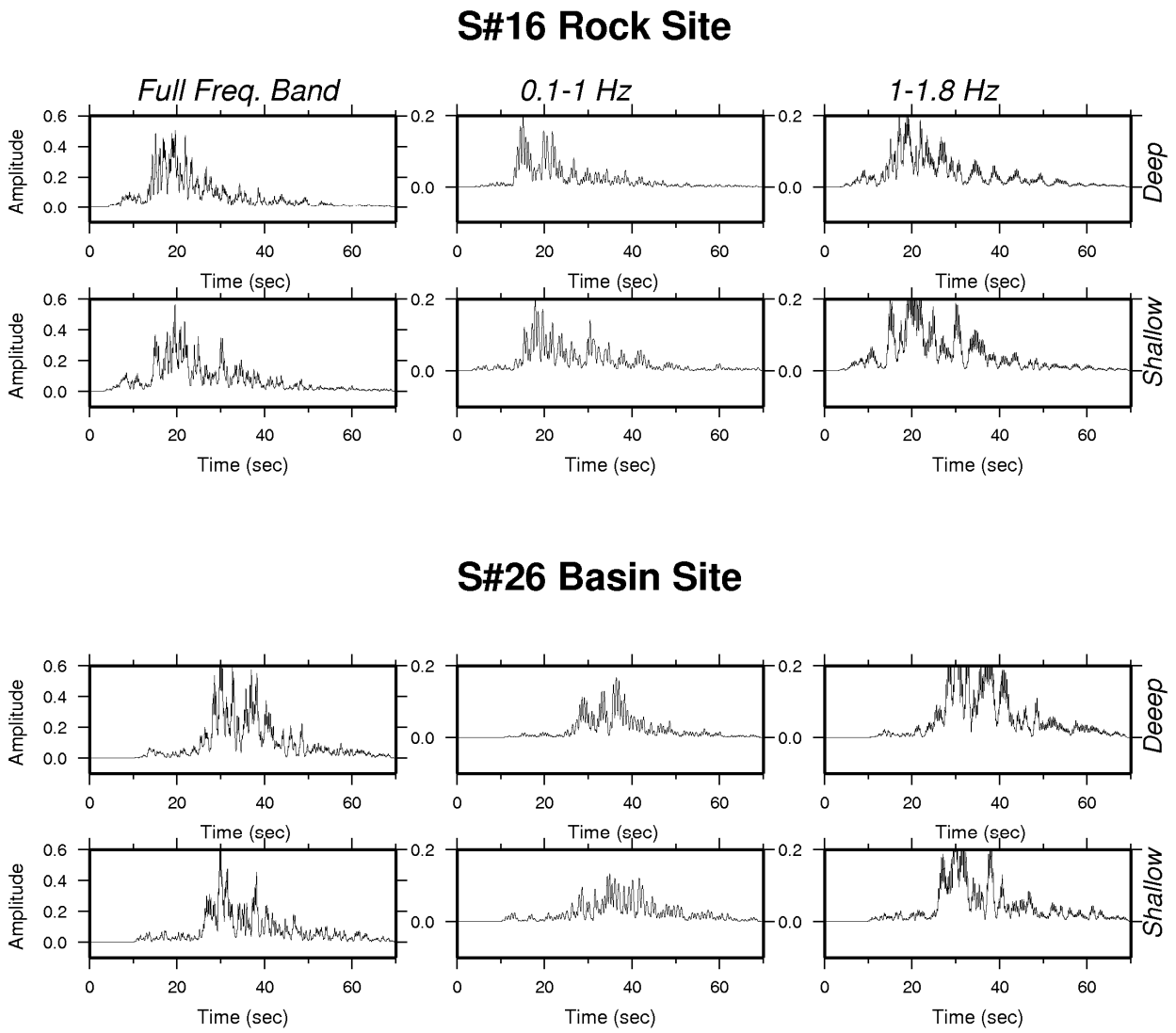

Figure 12. Smoothed envelopes of synthetic seismograms at sites S16 and S26. The envelopes are calculated using the vertical component of synthetic velocity seismograms band-pass filtered at 0.1-1.8 Hz (left panels), 0.1-1 Hz (middle panels), and 1-1.8 Hz (right panels). The difference in the envelope slope for scattered S waves from deep and shallow sources is noticeable at low frequencies only. At high frequencies the slope remains unchanged suggesting a stable shallow scattering effect**.**

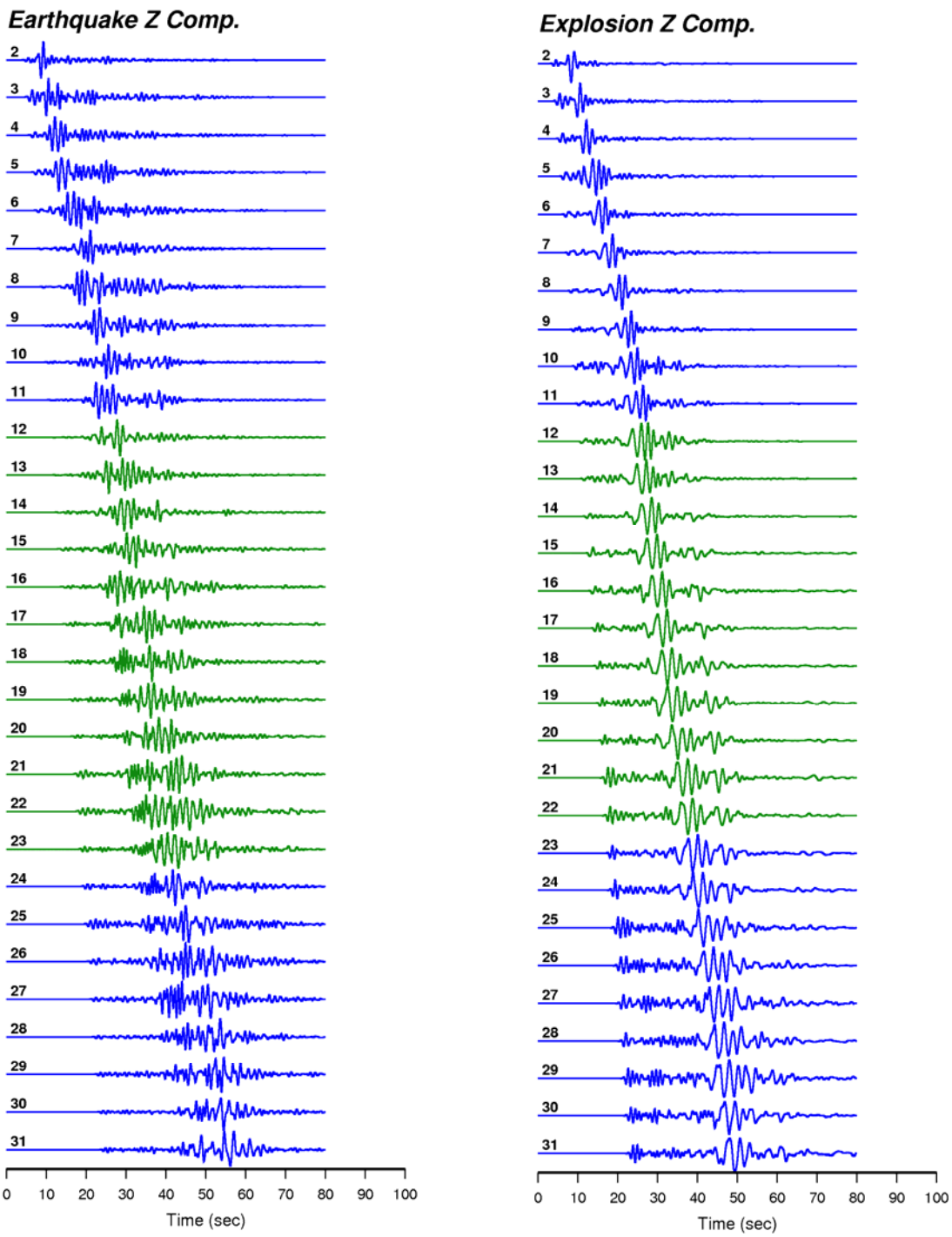

Figure 13a. Vertical component of synthetic velocity for a strike-slip earthquake with a source depth of 2 km (left panel), and isotropic explosion source at a depth of 0.4 km (right panel) band-pass filtered at 0.1-1.0 Hz. The synthetics are scaled to their individual maximum amplitude in order to facilitate the amplitude comparison between P and S waves at each station. Blue traces correspond to basin sites and green traces correspond to rock sites.

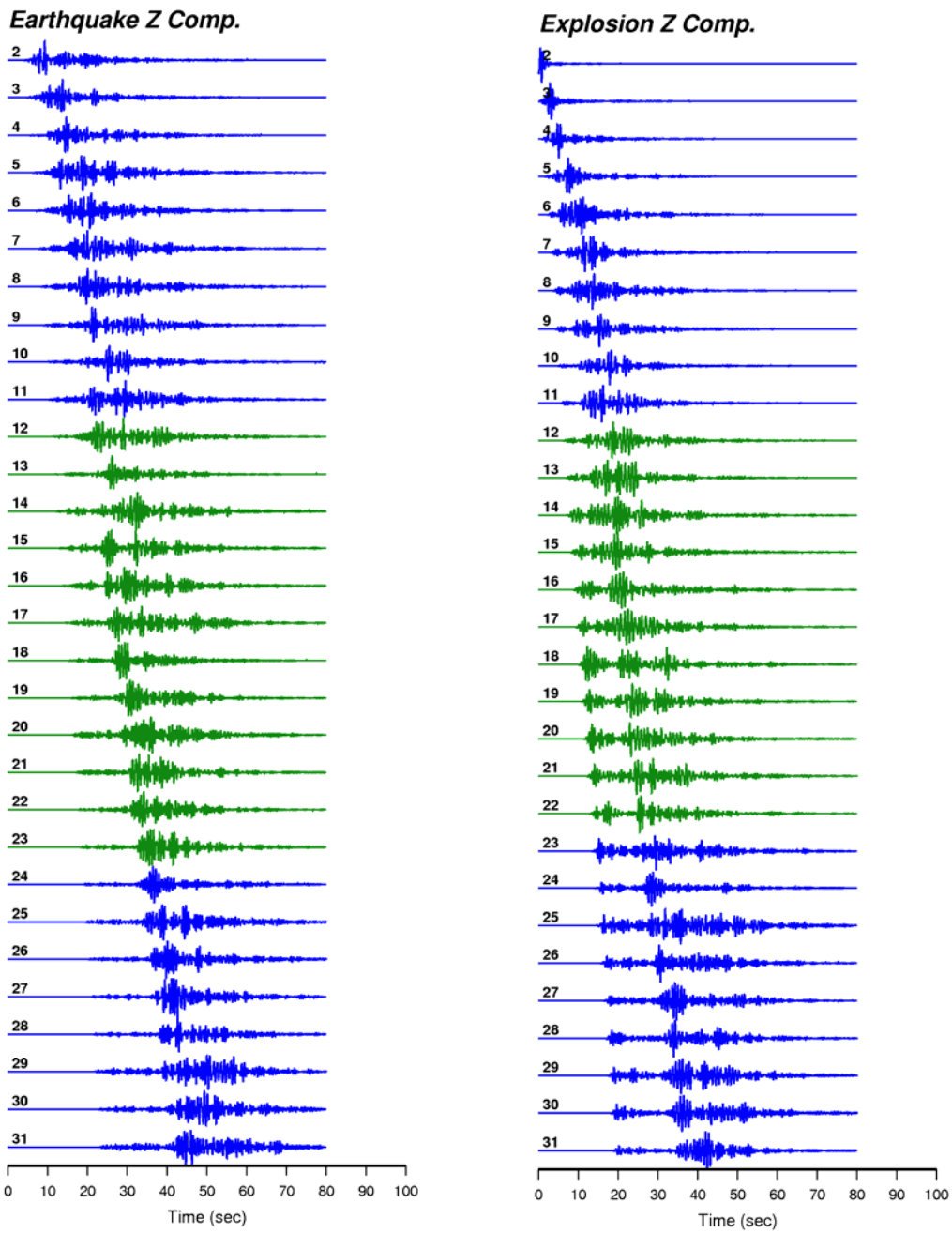

Figure 13b. Same as Figure13a but band-pass filtered at 1.0-1.8 Hz. The synthetics are scaled to their individual maximum amplitude in order to facilitate the amplitude comparison between P and S waves at each station.

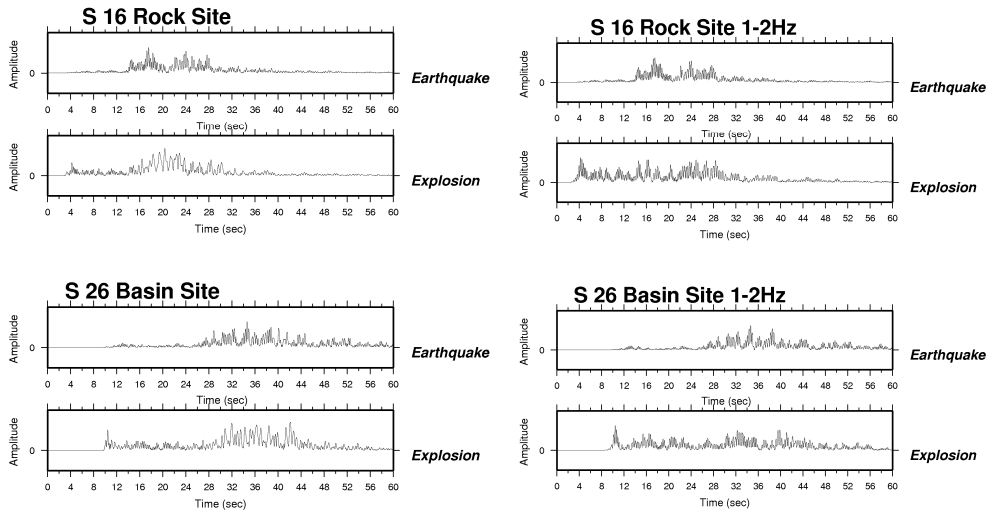

Figure 14. Comparison of smoothed envelopes for the vertical component of synthetic velocity seismograms at a rock site (station 16) and basin site (station 26) for earthquake and explosion sources, band-pass filtered at 0.1-1 Hz (left panels), and 1-1.8 Hz (right panels). Note the relatively large P/S ratio of coda waves for the explosion in the frequency band 1-1.8 Hz. The simulated P/S ratio increases with frequency. This is in good agreement with observations.

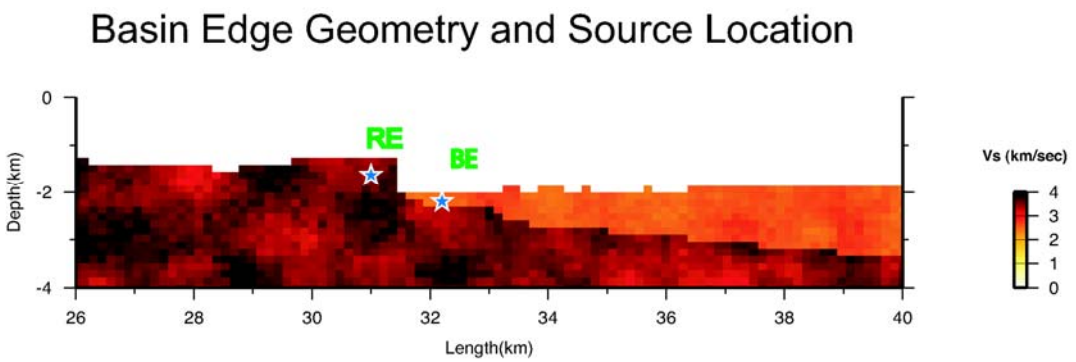

Figure 15. Close up of the velocity model in the region near the basin edge. Blue stars indicate the location of the explosion sources in rock near (RE) and in the basin sediments (BE) used in the simulations.

Basin Edge **Rock** **Basin Edge**

Rock

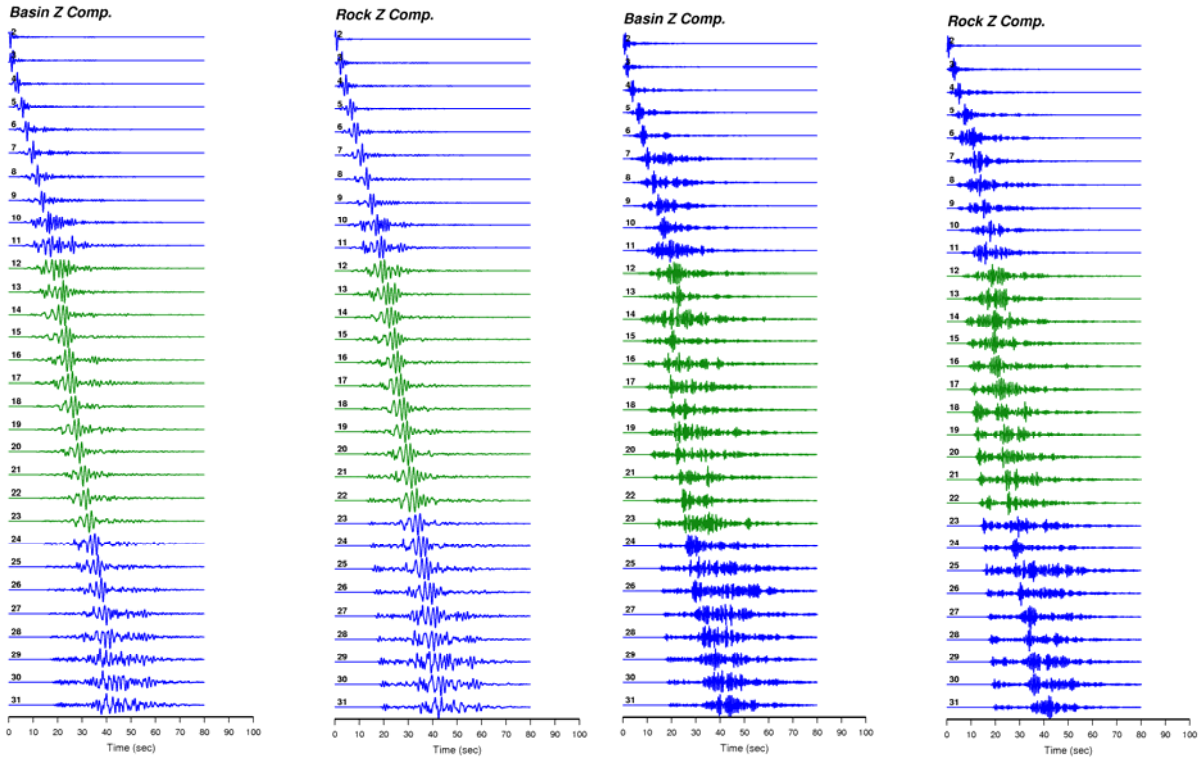

(0.1-1.0 Hz) **(1.0-1.8)Hz**

Figure 16. Vertical component of synthetic seismograms calculated at the linear array shown in Figure 10 for an explosion source embedded in rock adjacent to the basin (Rock), and an explosion source embedded in basin sediments next to the basin edge (Basin Edge). Left panels show synthetic seismograms band-pass filtered at 0.1-1.0 Hz, and right panels show synthetic seismograms band-pass filtered at 1.0 -1.8 Hz. There is a significant difference in the amplitude of high frequency coda waves (1-1.8 Hz) between the two sources. Note that the basin edge explosion source generates weaker P waves but stronger S coda waves

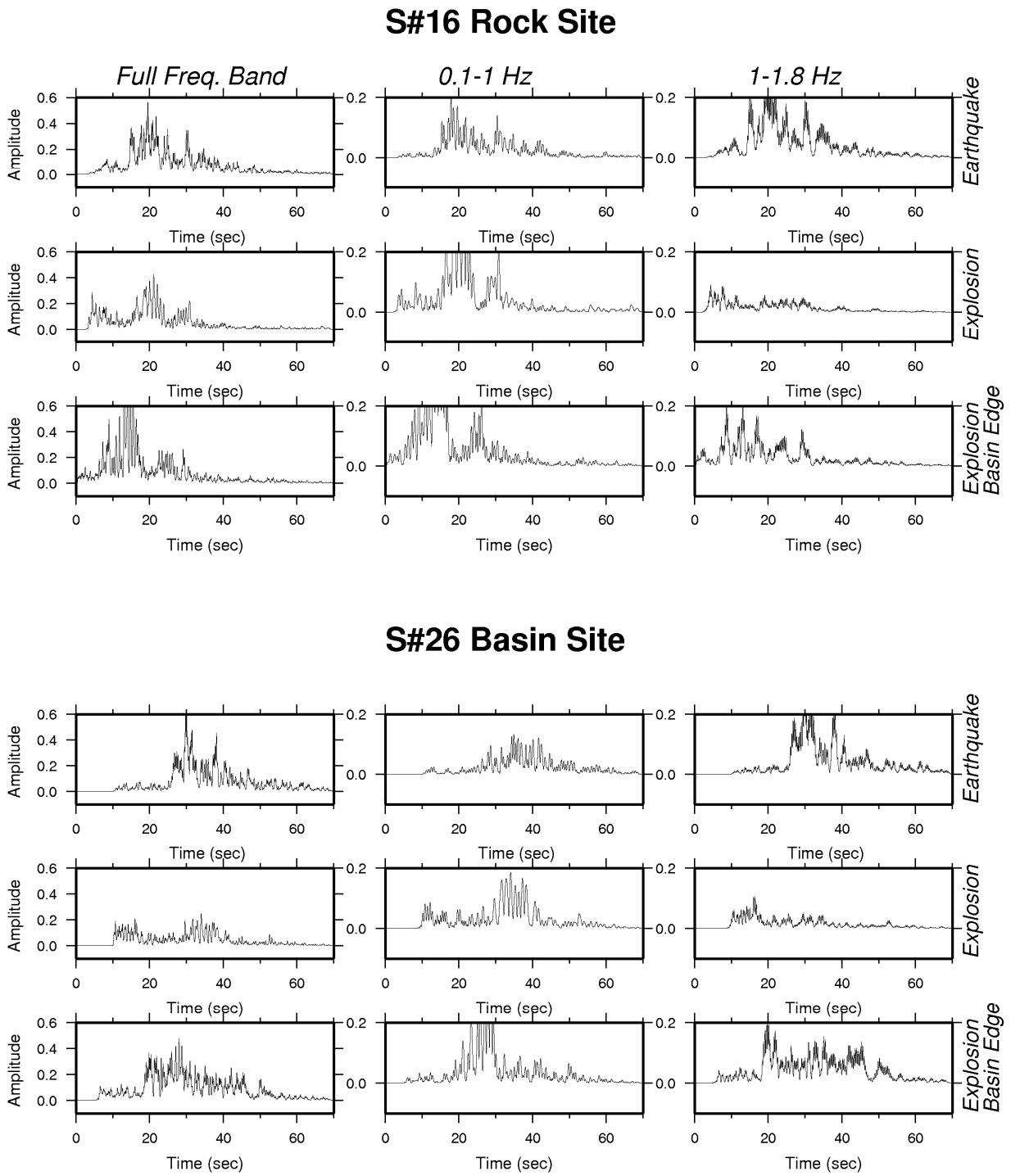

Figure 17. Comparison of smoothed envelopes of the vertical component of velocity calculated at station S16 (left panels) and station S26 (right panels) between an earthquake at a depth of 7 km, an explosion located outside the basin at depth of 400m (RE), and an explosion located within the basin at a depth of 400 m (BE). In contrast with the rock explosion, the waveforms from the basin explosion look very similar to the waveforms from the earthquake in both rock and basin sites.

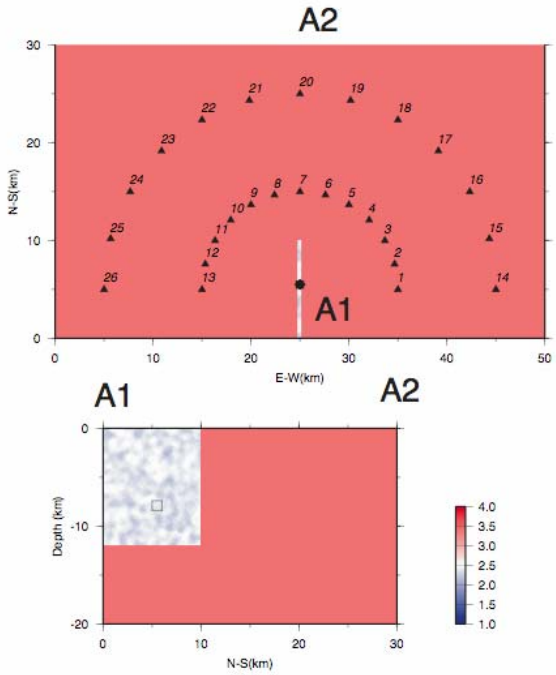

Figure 18. Top panel: Surface view of a vertical fault zone and station locations. Bottom panel: Cross-section of the 3D model across the fault zone along line A1-A2. The velocity heterogeneity in the fault zone is modeled by perturbing the shear modulus by +/- 10% with a correlation length of 1 km. The small rectangle shows the location of a 1km x 1km fault used in the simulations of rupture directivity.

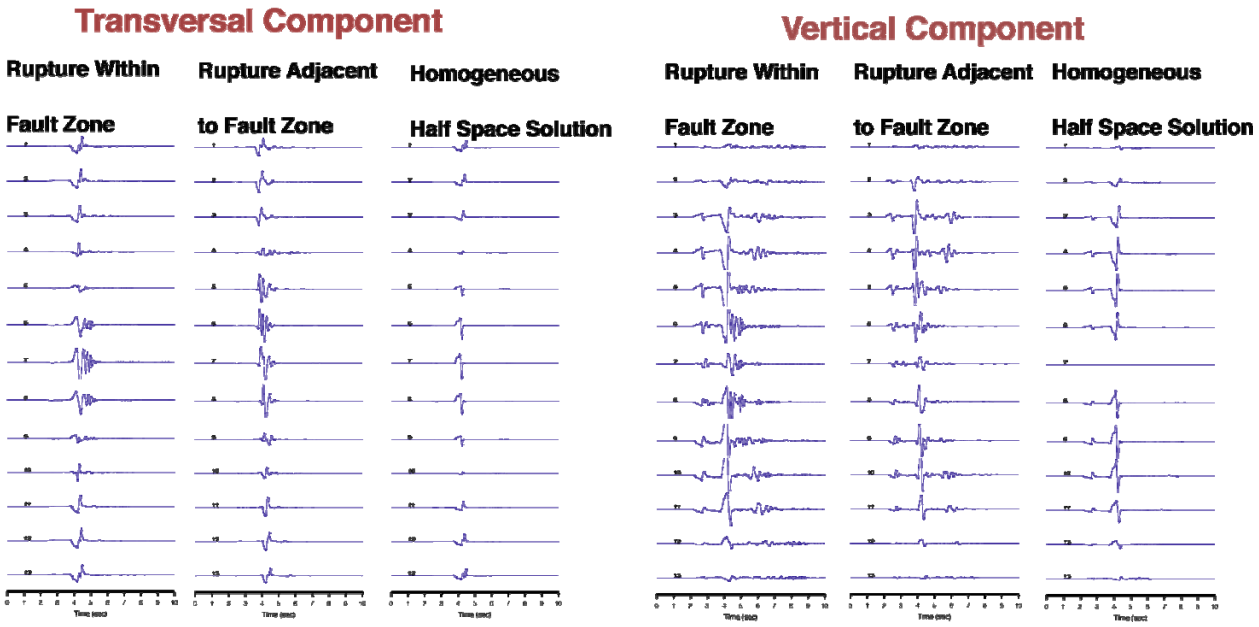

Figure 19. Tangential component (left panels) and vertical component (right panels) of finite-difference synthetic velocity seismograms band-pass filtered at 0.1-7Hz. The station number is indicated on the left of each trace. The small fault ruptures toward the north. We considered three scenarios; fault located in the fault zone, fault located next to the fault zone and a reference scenario for a fault embedded in a homogeneous half space. The S wave pulse is sharper when the earthquake ruptures outside the fault zone. The fault zone structure mostly affects the S wave. The effect on the P wave is insignificant.

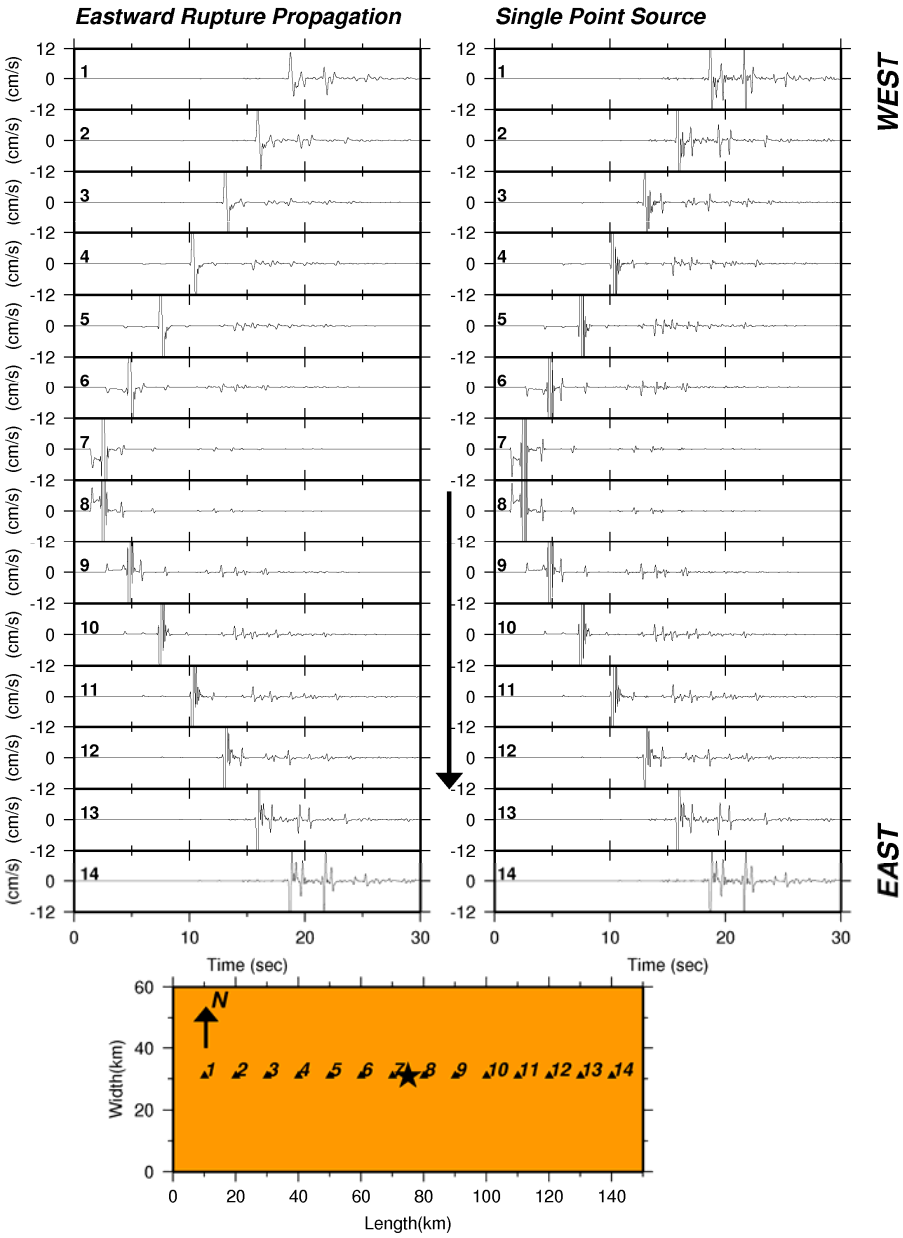

Figure 20a. Rupture directivity at a linear array of stations simulated using 4 double-couple point sources with pure strike-slip mechanism, activated at equal time intervals to simulate unilateral rupture propagation. We used a reference 1D layered model to simulate velocity seismograms up to 6.5Hz.

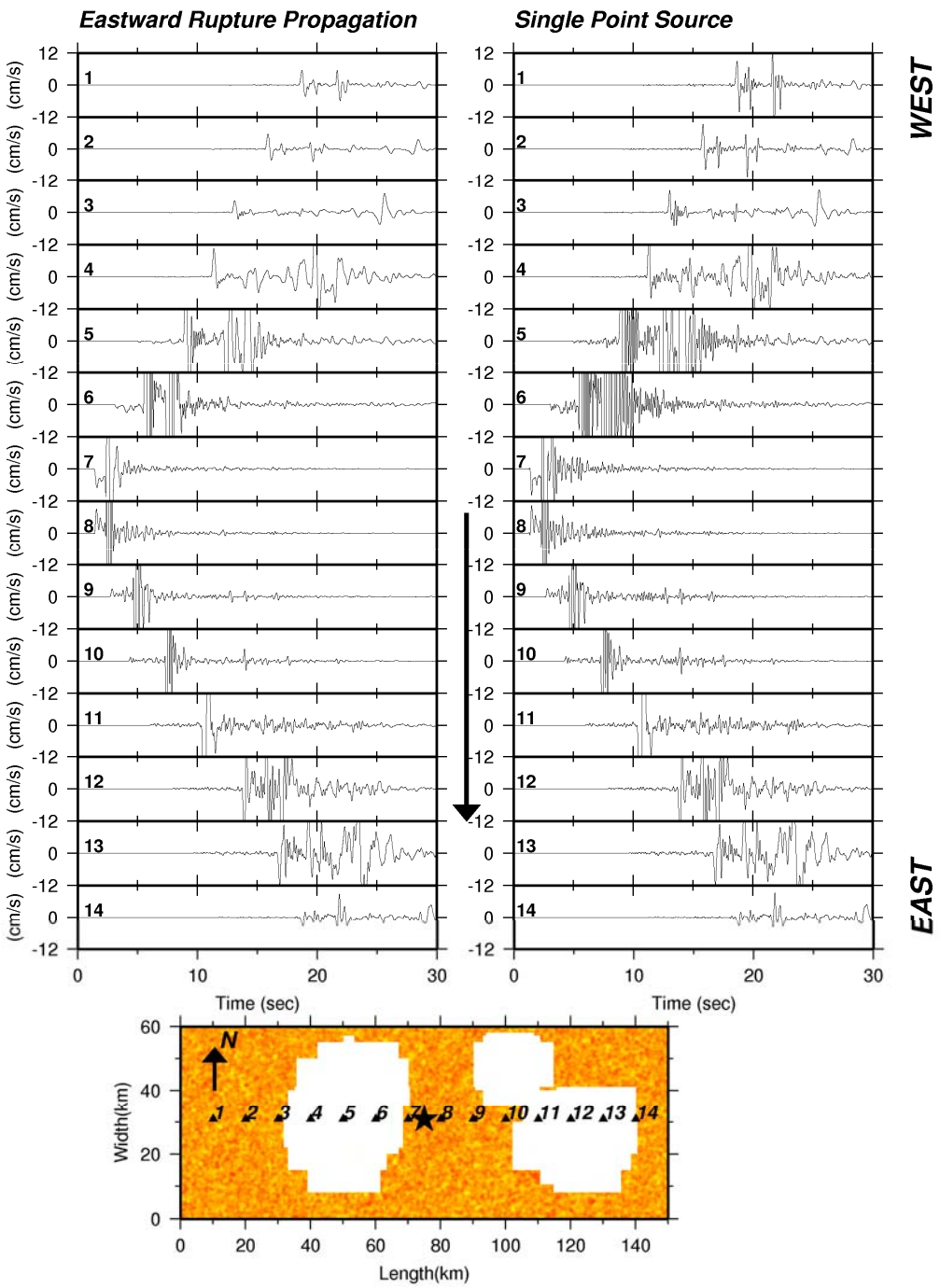

Figure 20b. Same as Figure 20a but for a 3D velocity model with velocity perturbations. The 3D velocity model used in the finite-difference simulations is the horizontally layered model with shallow basins, and random perturbations in the upper 6 km.

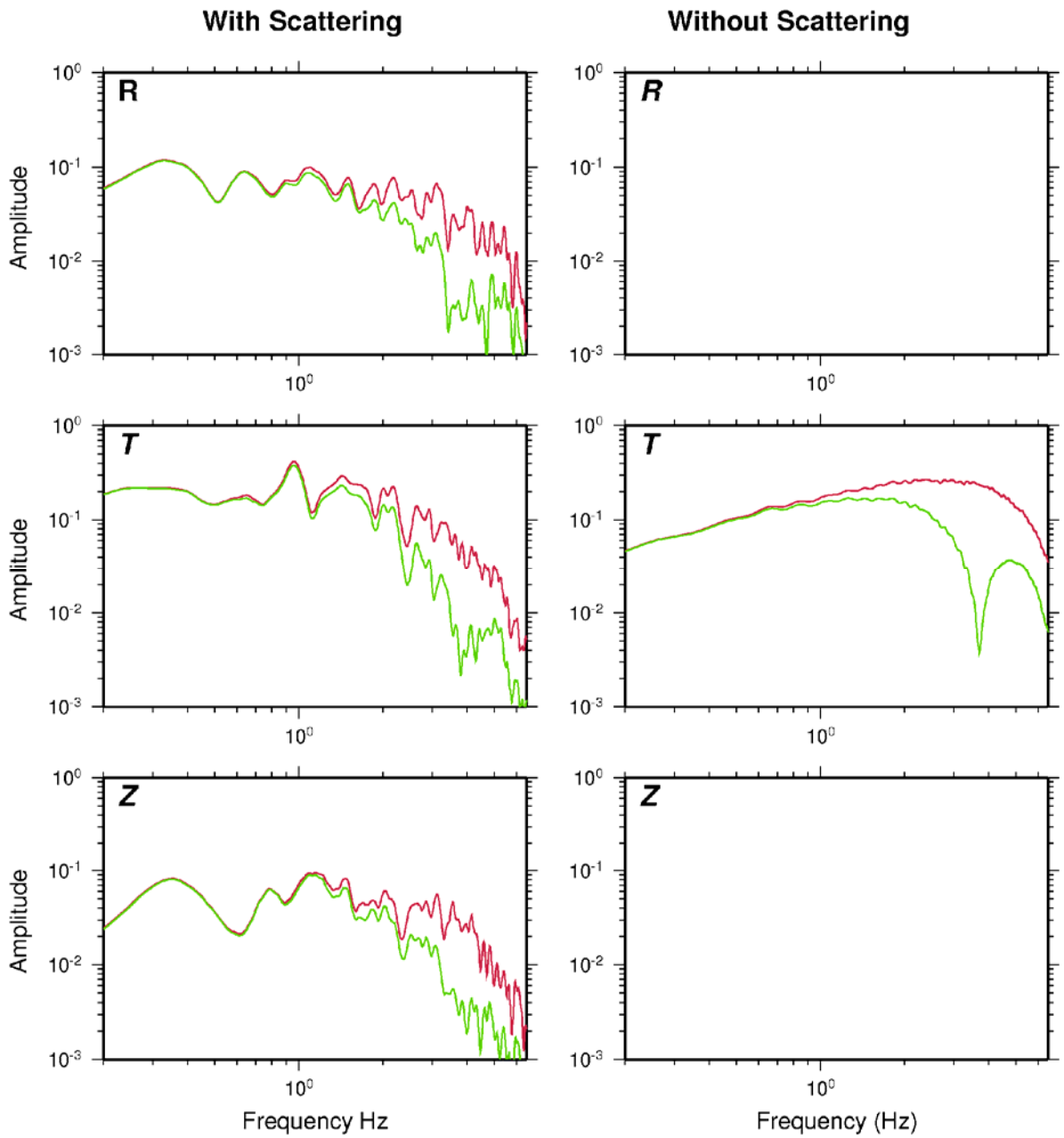

Figure 21. Comparison of Fourier amplitude spectra of velocity calculated at station 12 which recorded forward rupture directivity (red trace) and station 4 which recorded backward rupture directivity (green trace). Left panels correspond to the 3D model with scattering, and right panels correspond to the 1D model. Scattering reduces the amplitude of high frequency motion, but it does not modify the backward and forward directivity effects of rupture propagation, expressed as difference in waveform between motions at stations with forward rupture directivity (station 12), and backward rupture directivity (station 4).

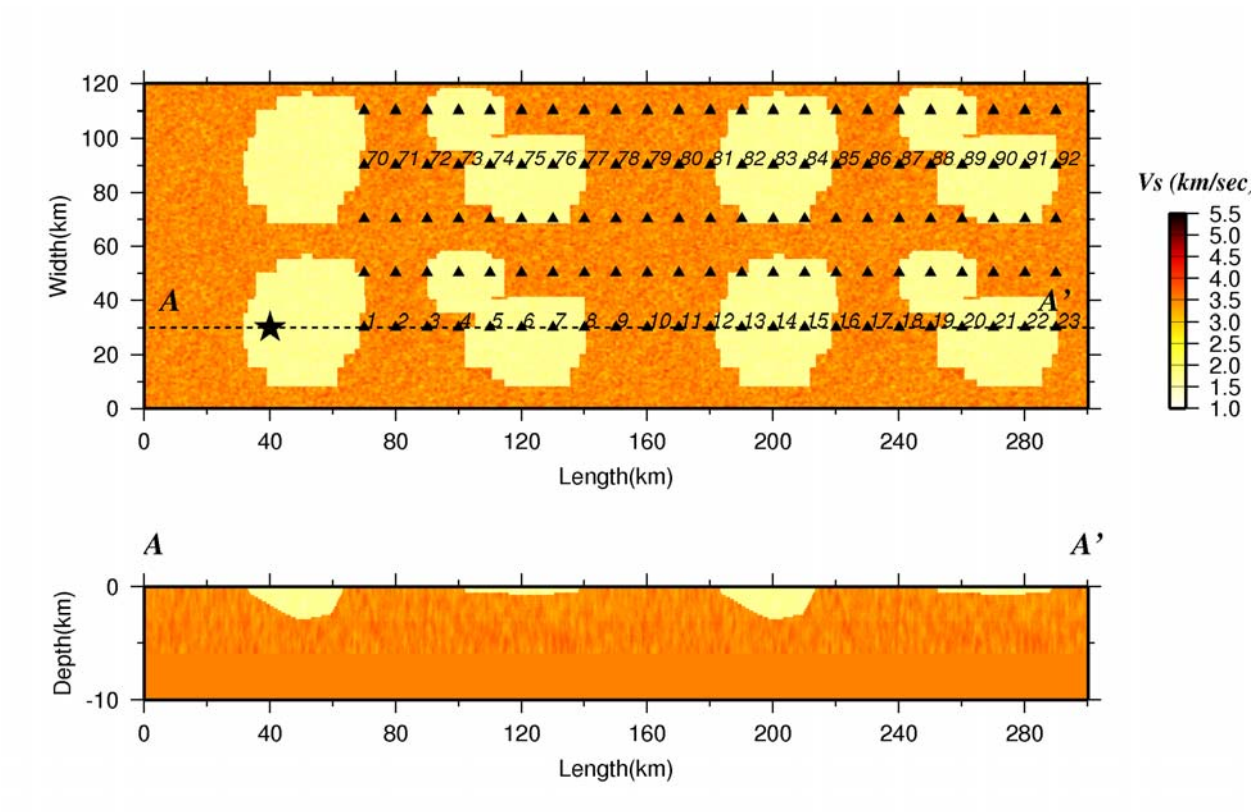

Figure 22. 3D regional velocity model used in modeling wave propagation scattering using a flat free surface. Top Panel: Free surface of the 3D velocity model. Yellow colored areas are shallow basins. Star indicates the hypocenter location of the source and triangles show the station locations. Bottom Panel: Top 10 km of a vertical cross section of the 3D velocity model along A-A' line.

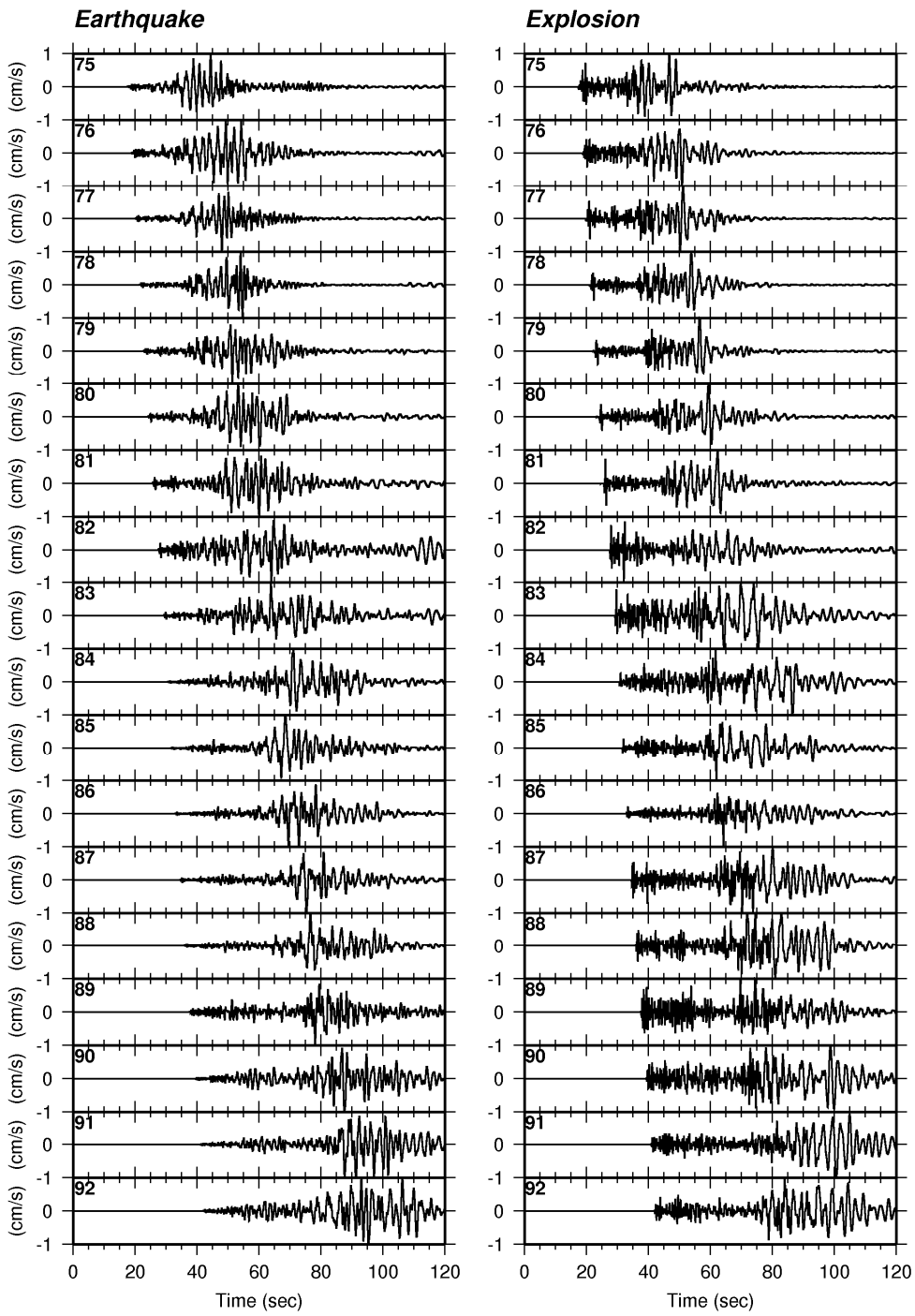

Figure 23a. Vertical component of synthetic velocity for a strike-slip earthquake with a source depth of 2 km (left panel) and an isotropic explosion source at a depth of 0.5 km (right panel) band-pass filtered at 0.1-3.5 Hz. All synthetics are individually scaled by their maximum amplitude.

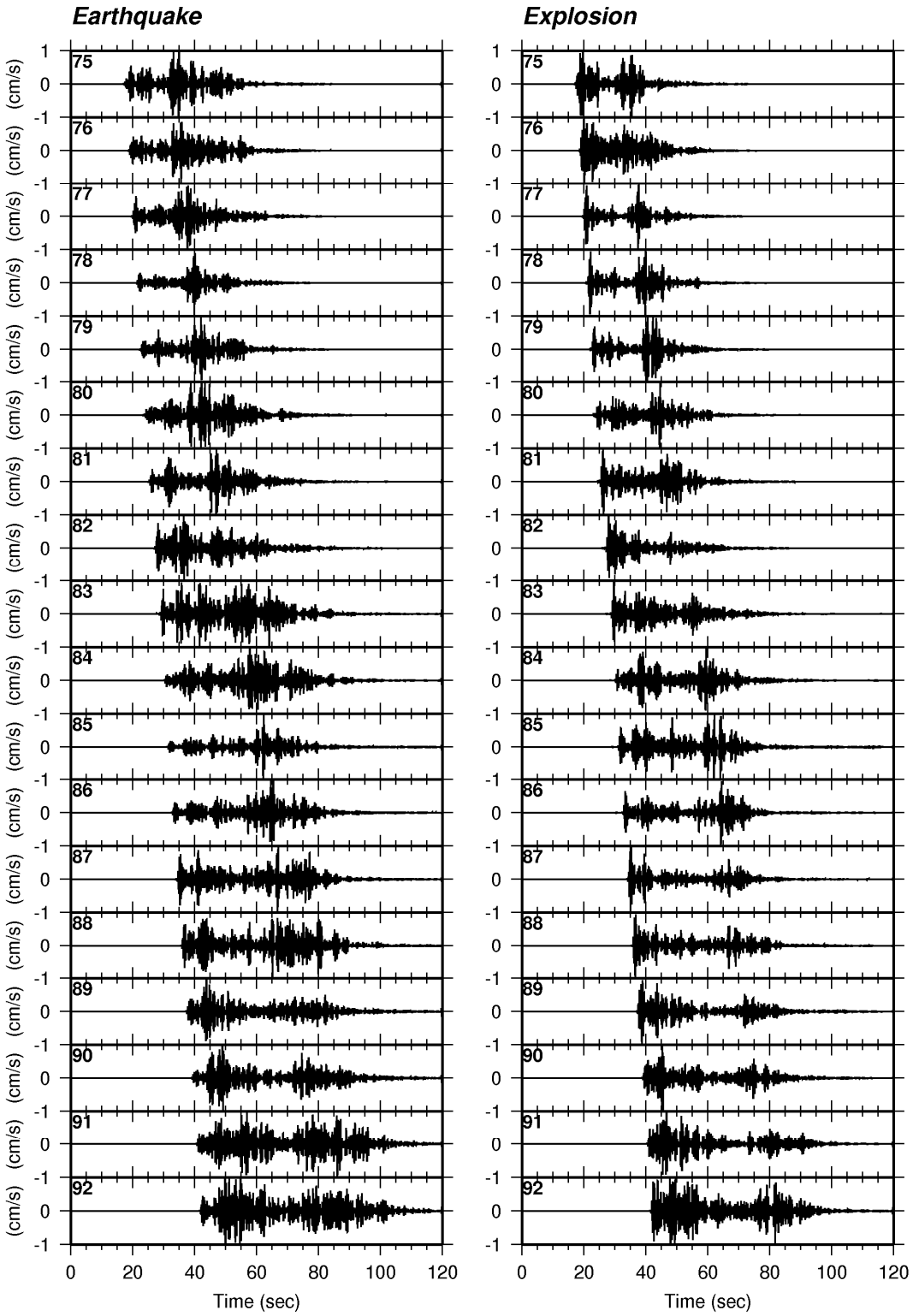

Figure 23b. Same as Figure23b but band-pass filtered at 2.0-3.5 Hz.

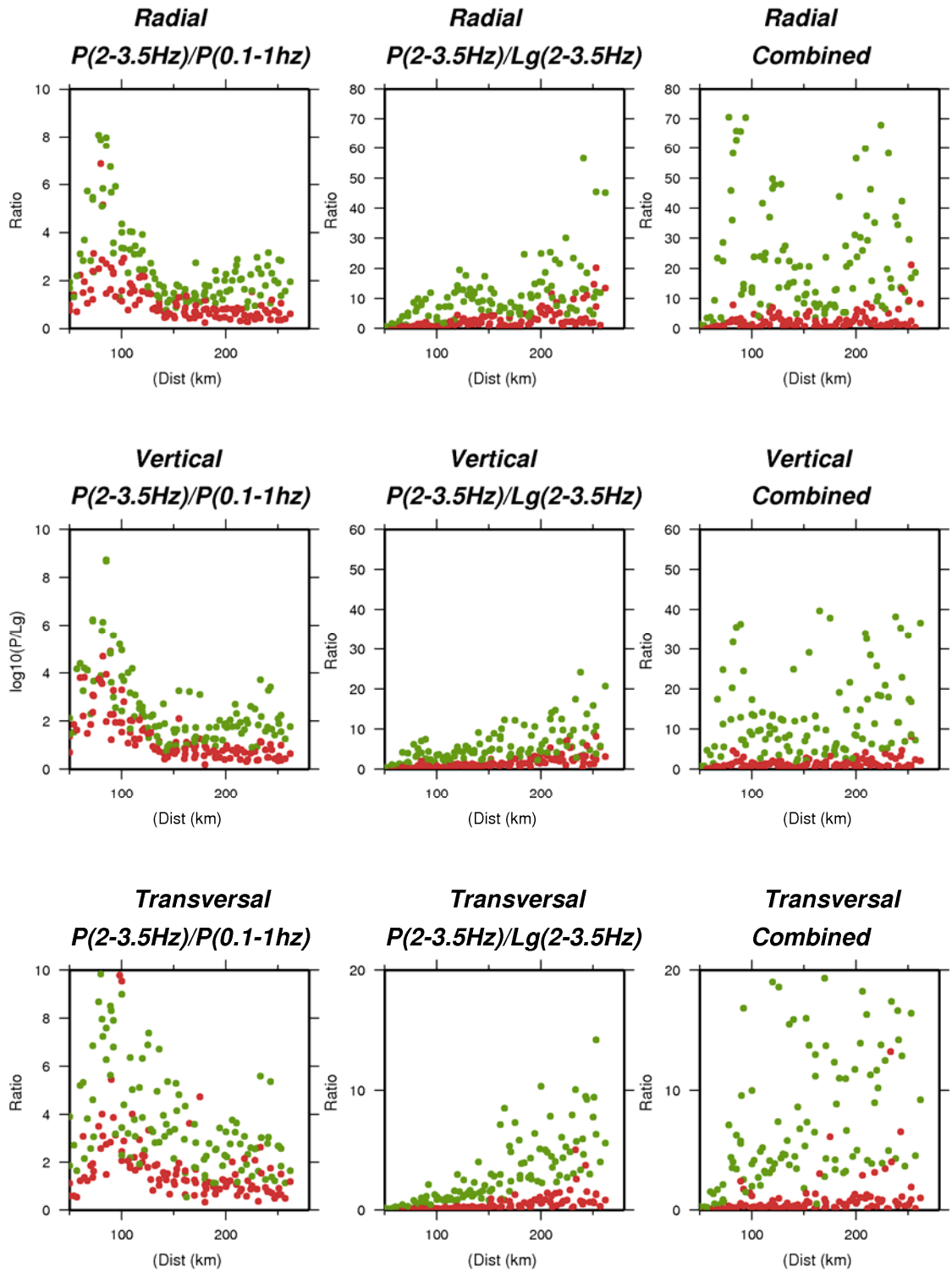

Figure 24. Simulated P(2-3.5Hz)/P(0.1-1.0Hz) ratios (left panels) P(2-3.5Hz)/Lg(2-3.5Hz) ratios (middle panels) and P(2-3.5Hz)/P(0.1-1.0Hz) *P(2-3.5Hz)/Lg(2-3.5Hz) ratios (right panels) for an explosion (green dots) and a shallow earthquake (red dots) for radial, transverse, and vertical components of waveforms. The synthetics are calculated with a 3D multilayer velocity model with random perturbations in the top 6 km. The velocity model is shown in Figure 22.